Glacial landscape and paleoglaciation in Terra Sabaea: Evidence for a 3.6 Ga polythermal plateau ice cap

Axel Bouquety, Antoine Séjourné, F. Costard, Sylvain Bouley, Eric Leyguarda

Glacial landscape and paleoglaciation in Terra Sabaea: Evidence for a 3.6 Ga polythermal plateau ice cap.

Axel Bouquety [a*], Antoine Sejourné [a], François Costard [a], Sylvain Bouley [a] & Eric Leyguarda [a]

a GEOPS, Univ. Paris-Sud, CNRS, Universit Paris-Saclay, Rue du Belvdre, Bt. 504-509, 91405 Orsay, France
**Corresponding author. E-mail address: a.bouquety@gmail.com (A.Bouquety).*

Abstract

In a previous study, we demonstrated with a comparative morphometrical analysis the first morphometric evidence of a glacial landscape composed of glacial cirques and glacial valleys in the south of Terra Sabaea at an elevation > 1000 m in two impact craters and one mountain. The purpose of this study is to use the same method to seek other geomorphologic evidence of glacial landscapes elsewhere in Terra Sabaea. Based on a comparison between current and old glacial landscapes on Earth and Mars, we identified 81 glacial valleys and possible evidence for a former plateau ice cap dated at 3.6 Ga at the highest elevation in Terra Sabaea. The identified glacial valleys have the same morphometric properties as terrestrial and martian glacial valleys with U-shaped cross-sectional profiles, a V-index > 0.2, a length to with ratio > 1 and a cross-sectional area to drainage area ratio four times higher than the fluvial ones. Moreover, these properties are different from terrestrial and martian fluvial valleys. We did not find well preserved glacial cirques in this area, this absence questions the origin of glacial valleys. However, the presence of an extensive flat plateau, from which the long valleys radiate, could have hosted an ancient plateau ice cap which was the source of these glacial valleys. A comparison with the Cantal and the Shaluli Shan in the southeastern Tibetan plateau on Earth reveals morphometrical similarities with our study area. In fact, long glacial valleys, originating radially from a plateau at higher elevation are characteristics of an ancient plateau ice cap. This analysis allowed us to propose a polythermal regime for martian glacial landscape, namely a cold-based ice cap except at the margin where the regime is warmed-based due to the steeper topography. This topography created shear stress which increased the heat at the base of the ice and created the outlet glacial valleys. Near the plateau, the radial valleys are U-shaped with a V-index > 0.2 but downstream, to the low elevation area, these valleys become more V-shaped with a V-index around 0.1. This hypothesis is supported by the presence of an open-basin paleolake making the transition between inlet glacial valleys upstream and an outlet V-shaped valley downstream. So the morphometry of the radiating valleys suggests that liquid water played a role in the formation of this landscape.

Keywords: Early Mars, Glacial landscape, Plateau ice cap, Morphometry

1 Introduction

The Early Mars climate is today one of the most debated subjects in the Mars research (Marsatwar,2018; Wordsworth et al., 2018) .On the one hand, the vision of an early wet and warm climate is suggested by the presence of valley networks and hydrated minerals which are the best lines of evidence for prolonged liquid water on Mars (Carr, 1995; Craddock and Howard, 2002; Bibring et al., 2006; Ramirez and Craddock, 2018). These valleys have V-shaped or U-shaped cross-profile shapes and are commonly inlet and outlet valleys of Noachian-aged basins (Fassett and Head, 2008b). The origin of the valley networks is still debated and four hypotheses are proposed: (1) precipitation-fed surface runoff (Craddock and Howard, 2002); (2) runoff fed by surface ice melting controlled by the climate (Segura, 2002); (3) runoff fed by surface or near surface melting by magmatic intrusions (Gulick, 2001); (4) sapping from subsurface aquifers (Carr, 1995). Whatever their formation process(es), the presence of valley networks similar to those on Earth show that during the Noachian (4.5-3.7 Ga), a hydrosphere was active on Mars with relatively warm and wet conditions. On the other hand, a new vision of an early cold climate, called "icy-highlands" is increasingly considered (Wordsworth et al., 2013, Forget et al., 2013, Bouley et al., 2016). This globally sub-zero scenario is suggested by climate modeling which indicates that with Noachian/early Hesperian conditions, namely an atmospheric pressure less than 1 bar, a reduced Tharsis bulge topography and a planetary spin axis obliquity of 45°, there is a preferential deposition of ice in the southern highlands at high altitudes > 1000 m (Forget et al., 2013, Wordsworth et al., 2013). These climate models are supported by geodynamic modeling which indicates that without the Tharsis dome, the valleys would be in a south tropical band from 40°S to 0°, the same distribution as observed today (Bouley et al., 2016). This tropical band is located in the same area where the ice could settle and accumulate following the climate modeling (Wordsworth et al., 2013, Head and Marchant, 2014, Bouley et al., 2016). So following these models, the valley networks could have been formed under a cold climate.

The "icy-highlands scenario" is often questioned, due to the presence of fluvial morphologies and deposits in the southern highlands (Bibring et al., 2006, Davis et al., 2016) and the difficulties to modelize an icy Mars with realistic conditions (Ramirez, 2017, Ramirez and Craddock, 2018). One of the main arguments against that scenario is the lack of geomorphologic evidence of glacial landscapes in Noachian terrains (Ramirez and Craddock, 2018). But, in a previous study, we demonstrated for the first time, with a detailed morphometrical analysis, the presence of glacial landscapes in the south of Terra Sabaea (42°17′E, 2°55′S) at elevations > 1000 m in two impact craters and one mountain (Bouquety et al., 2019). These glacial landscape comprise glacial cirques linked with glacial valleys (Fig.1). The glacial landscapes in Terra Sabaea have the same morphometric characteristics and trends as terrestrial and martian glacial valleys and cirques (Bouquety et al., 2019). They are also very different from those observed in fluvial valleys on Earth and Mars.

The purpose of this paper is to extend our study to other morphologies in three craters in Terra Sabaea (Fig.2), using the same morphometric method described in (Bouquety et al., 2019) and, to extend our understanding of the distribution at types of glacial landscape elsewhere in Terra Sabaea. We performed a comparison between morphologies found in this area and paleoglaciations found on Earth. By studying the morphometry of the valleys, we hope to define what was the paleoenvironnement in the south of Terra Sabaea 3.6 Ga.

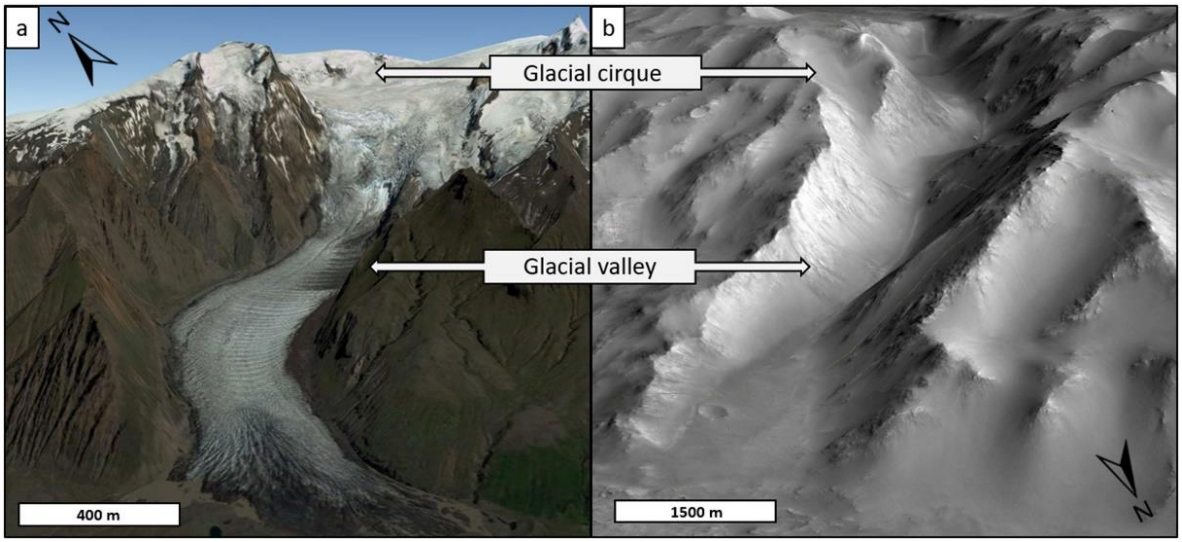

Figure 1: Comparison between glacial landscapes of (a) the Svinafell glacier in Iceland on Earth and (b) Dawes crater on Mars. Images credit Google Earth.

2 Paleoglacial landscape on Mars and Earth

2.1 Characteristics of identified glacial valleys and glacial cirques in Terra Sabaea: A 3.6 Ga glacial landscape

The highlands in Terra Sabaea exhibit several glacial landforms including 100 glacial cirques and 83 glacial valleys in two impact craters (Dawes crater, 42°17′E, 2°55′S, and crater 1, 42°34′E, 9°10′S) and one mountain in Terra Sabaea ((Bouquety et al., 2019); Fig. 2).This morphometric analysis allowed us to identify several characteristics of the valleys: (1) the glacial valleys have a U-shape with a wide flat floor and a V-index around 0.20 characteristic of glacial erosion while the fluvial morphologies have a V-shape with a V-index around 0.07 (Bouquety et al., 2019). (2) They have a length to width ratio >1 which is more similar to known terrestrial and martian hypothesised glacial valleys than fluvial valleys which have a length to width ratio >>1 (Hobbs et al., 2016, Bouquety et al., 2019). (3) The glacial valleys in Terra Sabaea have cross-sectional areas that are four times larger than martian fluvial valleys. This value of four is the characteristic difference between the glacial and fluvial valleys on Earth (Montgomery, 2002). (4) They respect the cross-section law, the cross-section area of the valleys increases down to the equilibrium line and then decreases downstream to the end of the valley, which is characteristic of terrestrial glacial valley (Penck, 1905). (5) They are located at higher elevation than the valley networks (> 1500 m). (6) They are dated between 3.34 and 3.66 Ga (Late Noachian/ Early Hesperian). (7) The valley heads in Terra Sabaea are often connected to the glacial valleys and they have morphological and geometrical similarities with the highest terrestrial glacial cirques measured by Barr and Spagnolo (2015) and Evans and Cox (2017).
To sum up, the measured characteristics are very similar to terrestrial glacial valleys and are very different from those ones from terrestrial and martian fluvial valleys. Today, we do not observe glaciers in the region of Terra Sabaea but relics of glacial landforms. The presence of these deglaciated landscape indicates that during the Late Noachian/ Early Hesperian, the climate was cold enough to have deposition of snow and preservation of ice leading to formation of glaciers and for the crater walls to be shaped by ice processes and form a glacial landscape (Bouquety et al., 2019).

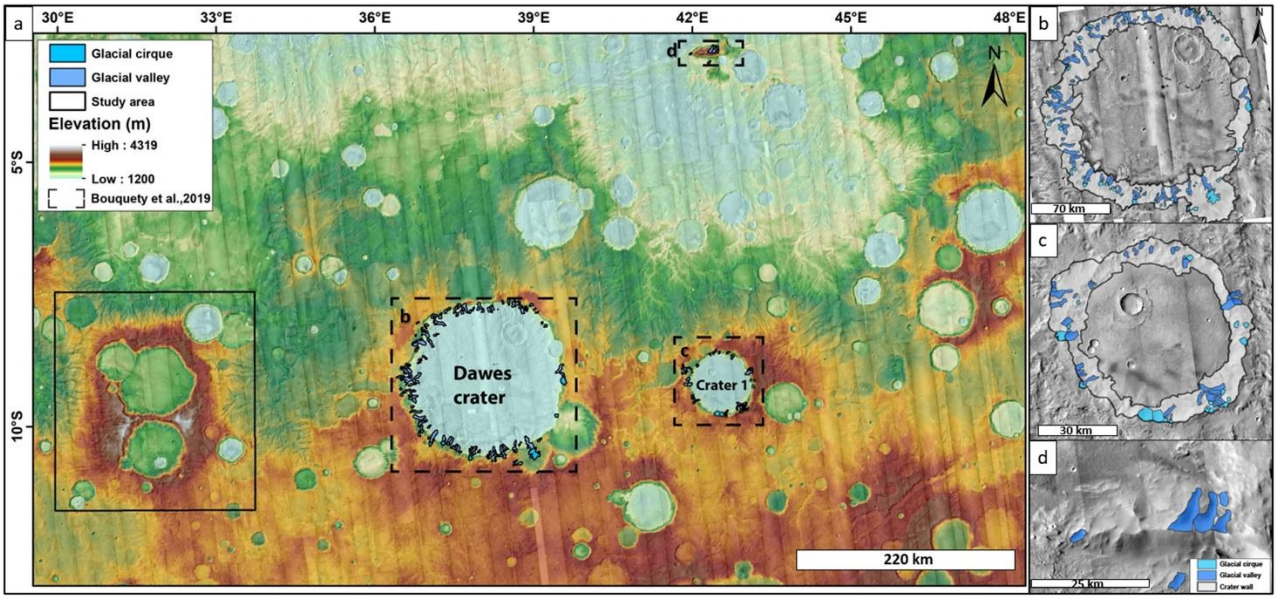

Figure 2: Location of the glacial landscape found in Terra Sabaea in Bouquety et al., (2019) represented by the doted black squares with associated zooms in (b), (c), and (d) The study area of this study is represented by the black square. Context camera (CTX) mosaic of the area with Mars Orbiter Laser Altimeter (MOLA) digital elevation map. Image credit NASA/JPL/University of Arizona.

2.2 Paleoglaciation on Earth: example from the Cantal in French Massif Central

Evidence of past glaciation has been extensively reported on Earth. In fact, variations of Milankovic parameters lead to glacial/interglacial cycles (Milankovitch, 1941). The last glacial phase was 80-100 ka ago (Larsen et al., 2006). The majority of ice was located at the poles, but evidence of glaciation has been found at mid-latitude, between 35°N and 50°N, in the Northern Europe. The region of the Cantal in the Massif Central in France was glaciated during this period ((Boule, (1896), Veyret, (1973), Valadas and Veyret, (1981)); Fig.3).

The Cantal is a stratovolcano which had been built by accumulation of lava from eruptions between 13 My to 2 My (Valadas and Veyret, 1981). The Cantal's morphology is shaped by vast basaltic plateaus formed by basaltic eruptions, these plateaus are called “planèze” (Boule, 1896). These planèze have a mean elevation of 1300 m and are cut by valleys which often start with an amphitheatre (Fig.3b). These valleys extend radially from the higher summit, around 1800 m, and follow the slope to the lowest elevation, around 200 m. In the lower elevation, the valleys join dense hydrographic network (Fig.3b). These valleys and amphitheatres have been identified by Boule (1896) as glacial landscape composed of glacial valleys and glacial cirques. Moreover, Boule (1896) and Veyret (1973) found several patterns of glacial erosion such as: (1) moraines, they are ridge-shaped deposits formed along the lateral margins of glaciers (Andersson, 1998, Ewertowski and Tomczyk, 2015). (2) Eskers which are a type of straight-to-sinuous ridge composed of sand and gravel resulting from the flow of glacial meltwater in predominantly subglacial and englacial conduits (Bennett and Glasser, 2011), and (3) drumlins which are a type of straight hills composed of sand and gravel deposited by the glacial recession (Bennett and Glasser, 2011).

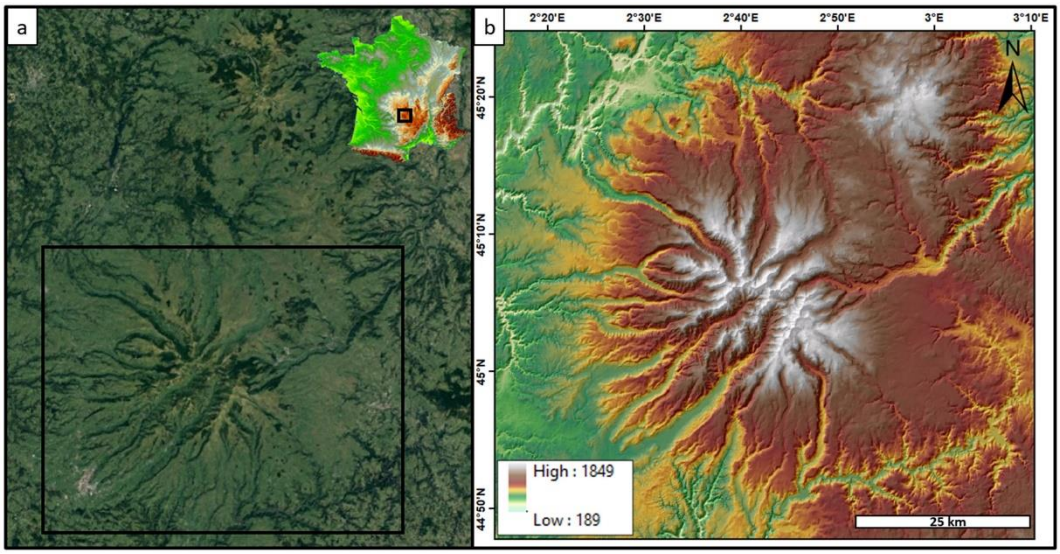

Figure 3: The Massif Central area. (a) Satellite photography of the area. The black rectangle represents the Massif du Cantal show in (b). (b) Colorized elevation data from 25m/pixel Digital Elevation Model (DEM). Images credit: Google earth and Institut national de l'information géographique (IGN)

The study of these erosion and deposit patterns indicate that the Cantal was glaciated during the last maximum glacial period (Fig.4; (Etlicher and Hervé, 1988)) The glacial landscape was, 12 My ago, composed of glacial cirques, glacial valleys and local plateaus ice cap on the planèze where their flat topography were favourable to a deposition and accumulation of ice (Boule, 1896, Veyret, 1973, Valadas and Veyret, 1981, Etlicher and Hervé, 1988). Today, the area is totally deglaciated, but the Cantal is still shaped by geomorphologic legacy of an old cold climate 12 My ago.

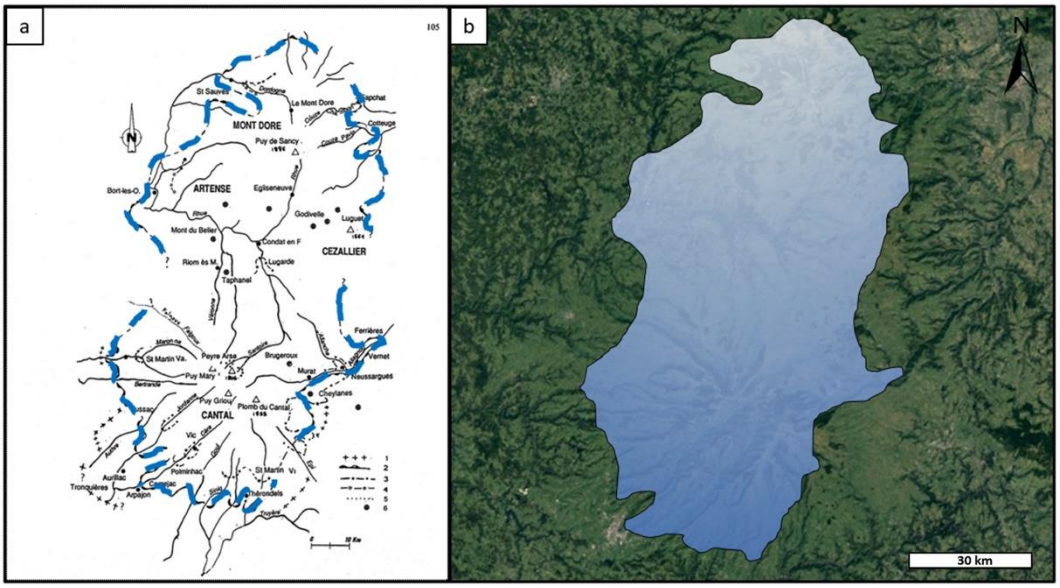

Figure 4: Reconstitution of the maximum glacial extend during the last glaciation in Cantal. (a) Morphological map modified from (Etlicher and Hervé, 1988). The blue lines are the limits of the maximal extend marked by the moraines. (b) Reconstruction of the assumed extent of ice draped on an aerial photography of the area. Image credits: Google Earth.

3 Study area

We focus our study on an area at the southwest of Terra Sabaea, between 8°S to 11°S and 31°E to 33°E (Fig.5a). This area is one of the highest parts of Terra Sabaea with a mean elevation at 3000 m above the reference MOLA datum and a summit at 4239 m. It belongs to the early Noachian highland unit (eNh, (Tanaka et al., 2014)). We can divide the area into three parts based on their relief: (1) the plateau is 22 km in average in width, has very gentle slopes and a mean elevation at 3150 m (Fig.6), it is the highest zone of the area (Fig.5a). The plateau does not show well marked morphologies such as valleys, but the slopes surrounding this plateau are shaped by many valleys mapped by Hynek et al., 2010 as valley networks (Fig.5e). (2) Three large size impact craters on the plateau. These craters are unnamed and will be called "crater 2" (41 km in diameter, Fig.5b), "crater 3" (92 km in diameter, Fig.5c) and "crater 4" (72 km in diameter, Fig.5d). (3) The radial valleys originate from the plateau, except for the south facing slope which does not presents valleys (Fig.5a). These valleys are referred to as "radiating valleys" for the rest of the study (Fig.5a, e).

4 Data and methods

4.1 Imagery

In order to understand the distribution and type of glacial landscapes at regional scale, we performed a comparative morphometrical analysis of the studied valleys with known cases on Earth and Mars. For Mars, we used Context Camera images (CTX) with a resolution of 6 m/pixel (Malin and Edgett, 2001) to characterize the valleys on Mars. Then, to constrain their geometry, we used the Digital Terrain Map Reduced Data Record (DTMRDR) data with 1 m numeric height resolution from High-Resolution Stereo Camera (HRSC) with a resolution of 10 to 50 m/pixel depending on the ground resolution of the respective image (Gwinner et al., 2016) and MOLA Mission Experiment Gridded Data Record, MEGDR with 463 m/pixel (Smith et al., 2001). We used both of these dataset because the global coverage of the HRSC DEM does not include all the study area and only cover Bakhuysen and Dawes crater. A map of the data availability is in the supplementary (Fig.24).We made our measurements using ArcGIS software. To measure the valleys on Earth, especially in the Cantal region in France, we used the 25 m/pixel DEM from the Institut national de l'information géographique (IGN). The projection systems used was "SimpleCylindrical_Mars" for CTX, with this projection, distortion increases as the distance from the standard parallels increases. We used "SINUSOIDAL_MARS" for DTMRDR, the scale along all parallels and the central meridian of the projection is accurate. And "Mars2000_ECylindrical_clon0" for MOLA. Our study areas are near the equator (between 2° and 9°S), which is a standard parallels so the distortions can be neglected.

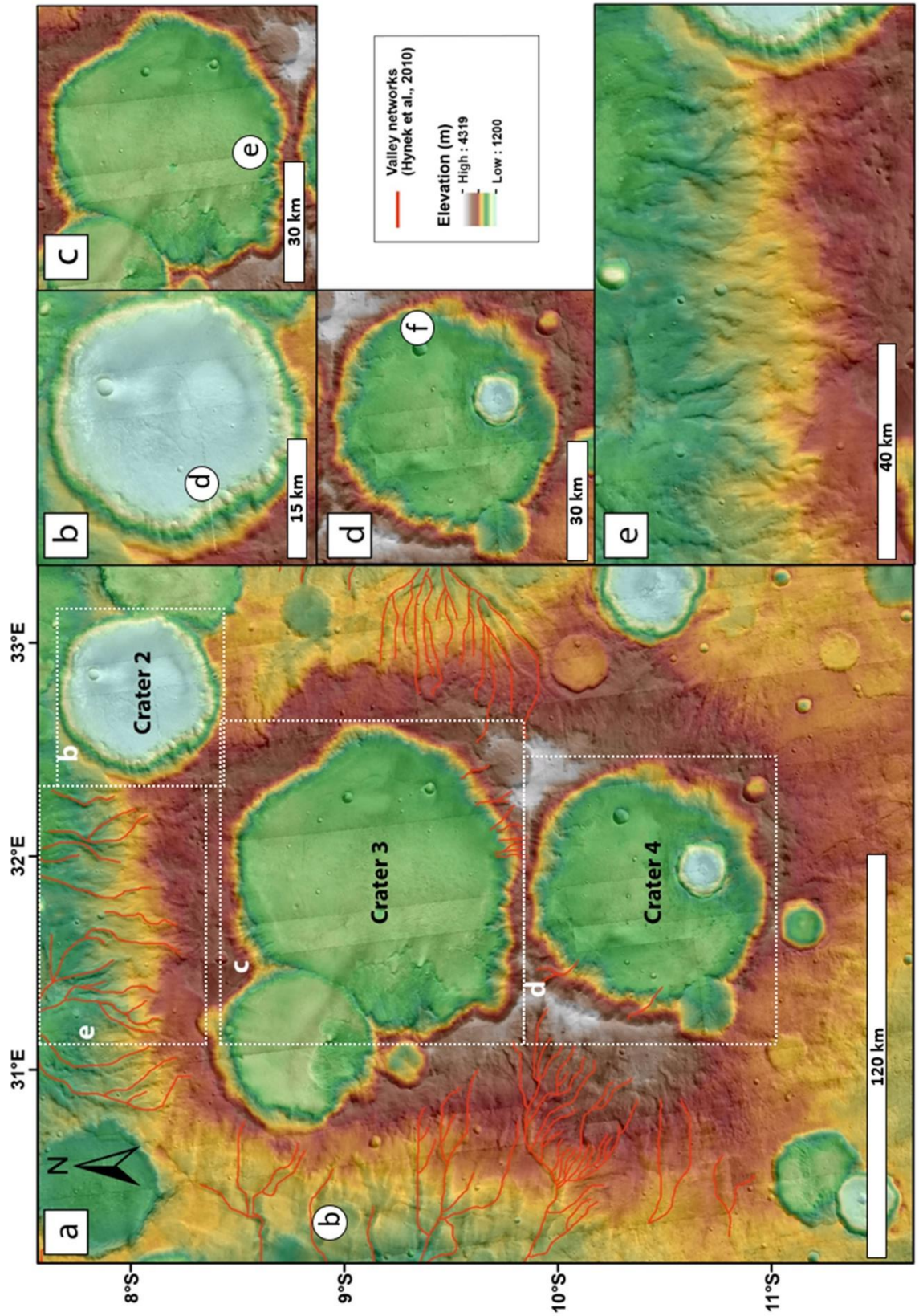

Figure 5: Area of interest in Terra Sabaea. (a) Study area, Context Camera (CTX) mosaic of the study area with MOLA digital elevation map. The red lines are the valley networks identified by Hynek et al., (2010). (b) Crater 2 CTX images with MOLA background. (c) Crater 3 CTX images with MOLA background. (d) Crater 4 CTX images with MOLA background. (e) Zoom in the north part of the plateau with the valleys flowing downstream, CTX images with MOLA background. The white circles are the valleys represented in the Fig.11. Images credit NASA/JPL/University of Arizona.

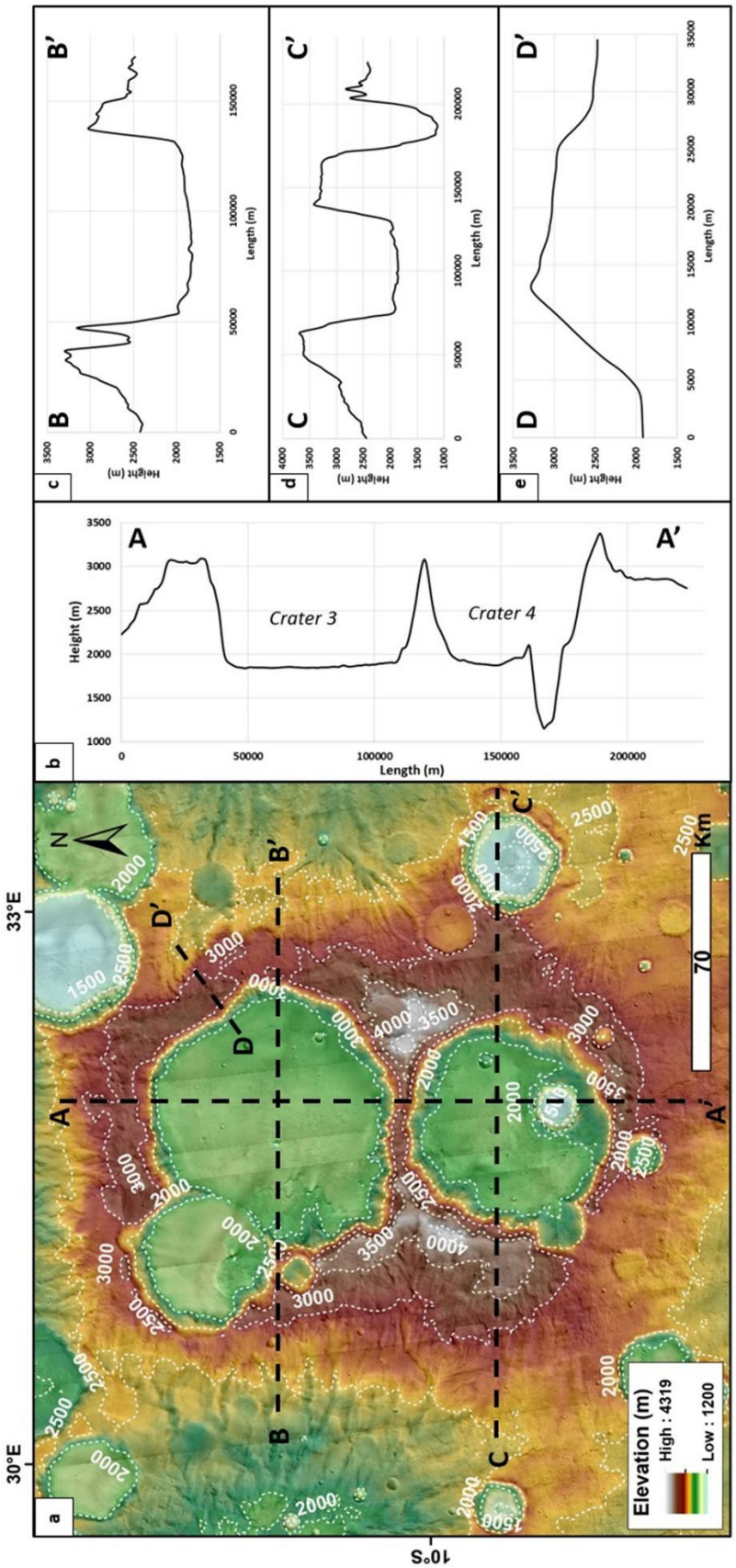

Figure 6: Plateau area. (a) CTX images with MOLA background. The dashed white lines are the topographic contours (500 m). The dashed black lines are the cross-section show in (b), (c), (d) and (e) from MOLA dataset. Images credit NASA/JPL/University of Arizona.

4.2 Morphometrical analysis of valleys on Mars

In order to define the erosive agent at the origin of the valleys, we used a morphometrical comparative analysis. We summarized all the parameters used to study the valleys on Earth and made a list of the morphometrical differences between terrestrial glacial and fluvial valleys. We measured as many parameters as possible to interpret the origin of the valleys (Table 1). For a much more detailed explanation of this method, the reader should refer to the section 4.3 of our previous paper (Bouquety et al., 2019).

Valley parameters	Abbreviation	Definition	References
Length (m)	L	Longitudinal line extending from the upstream part to the downstream part.	Johnson (1904), Roberts and Rood (1984), Livers and Wohl (2015), Hobbs et al., (2016)
Width (m)	W	Perpendicular to the length line.	Johnson (1904), De Martonne (1910), Roberts and Rood (1984), Livers and Wohl (2015), Hobbs et al., (2016)
Slope (°)	Sl	Average values of all pixels in the valley shape.	Montgomery (2002), Amerson et al. (2008)
Elevation (m)	El	Average values of all pixels in the valley shape.	Johnson (1904), Penck (1905), de Martonne (1911), Graf (1970), Roberts and Rood (1984), Augustinus (1992), Montgomery, 2002, Amerson et al., (2008), Zemp et al. (2011), Livers and Wohl (2015), Zimmer et al.(2018)
Depth (m)	Dp	Difference between the highest and lowest point from a cross-sectional profile.	Graf (1970), Roberts and Rood (1984), Augustinus (1992), Montgomery, 2002, Amerson et al., (2008), Livers and Wohl (2015)
Drainage area	Da	Surface delimited by the crests of the valley.	Penck, 1905, Graf (1970), Roberts and Rood (1984), Augustinus (1992), Montgomery, 2002, Amerson et al., (2008), Zemp et al. (2011)
V-index (dimensionless)	V-index	Deviation from an ideal V-shaped valley.	Zimmer et al., 2018
Cross-section (m^2)	CS	Calculated from the cross-sectional profiles.	Penck, 1905, De Martonne (1911), Graf (1970), Roberts and Rood (1984), Augustinus (1992), Montgomery, 2002, Amerson et al., (2008), Livers and Wohl (2015)
Length/width ratio (dimensionless)	L/W	Length/ width.	Hobbs et al., 2016

Table 1: Parameters measured for the valleys used in this study. Selected from several terrestrial studies. V-index= (Ax/Av)-1 with (Ax) the valley cross-sectional area and (Av) ideal V-shaped cross-section with the same height and width as the subject cross section. (Zimmer et al., 2018)

4.3 Comparative morphometrical analysis with known valleys on Earth and Mars

4.3.1 Comparison with Mars

We compared our results with two craters that have already been studied. These craters have been chosen as references for our comparison. The first, Bakhuysen crater (15.39°E, 23.9°S) has 35 valley networks mapped by Hynek et al., (2010) and are interpreted as fluvial valleys by Moore (2005) (Fig.7).The second is Dawes crater (42°17'E, 2°55'S), its inner walls has 42 valleys and 75 valley heads that have been interpreted as glacial valleys and glacial cirques by (Bouquety et al., 2019) (Fig.8).

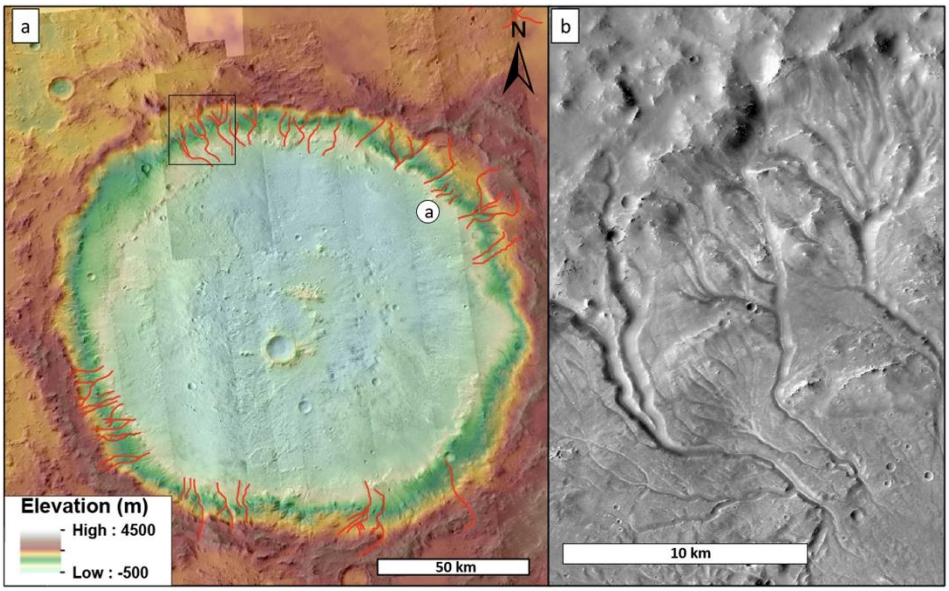

Figure 7: Bakhuysen crater (a) Background using CTX images and MOLA elevation data. The red lines represent the valley networks (Hynek et al., 2010). (b) CTX detailed view of the fluvial valleys shown in (a). Modified from (Bouquety et al., 2019). The white circle is the valley represented in the Fig.11 Image credit NASA/JPL/University of Arizona.

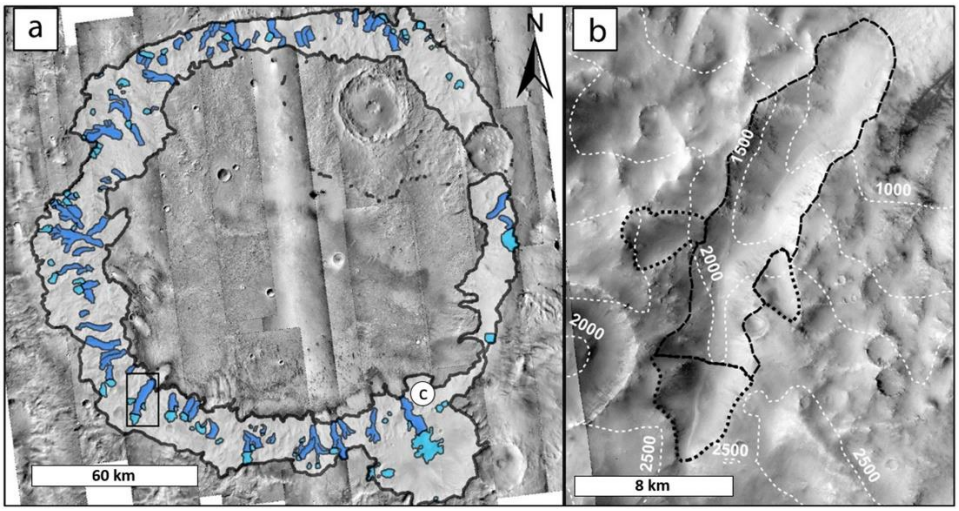

Figure 8: Dawes crater (a) Background using CTX images. The dark and light blue represents respectively the glacial valleys and the glacial cirques. (b) CTX detailed view of the glacial valleys surrounding by three glacial cirques shown in (a). Modified from (Bouquety et al., 2019). The white circle is the valley represented in the Fig.11. Images credit NASA/JPL/University of Arizona.

4.3.2 Comparison with the Earth

We decided to apply our morphometrical analysis to the region of Cantal in France (Fig. 9). The Cantal is volcanic region where evidence of past glaciation has been identified (Boule, 1896, Durand, 1939, Veyret, 1973, Valadas and Veyret, 1981). The fact that this area is totally ice-free and the basaltic composition make this region a good analogue for Mars.

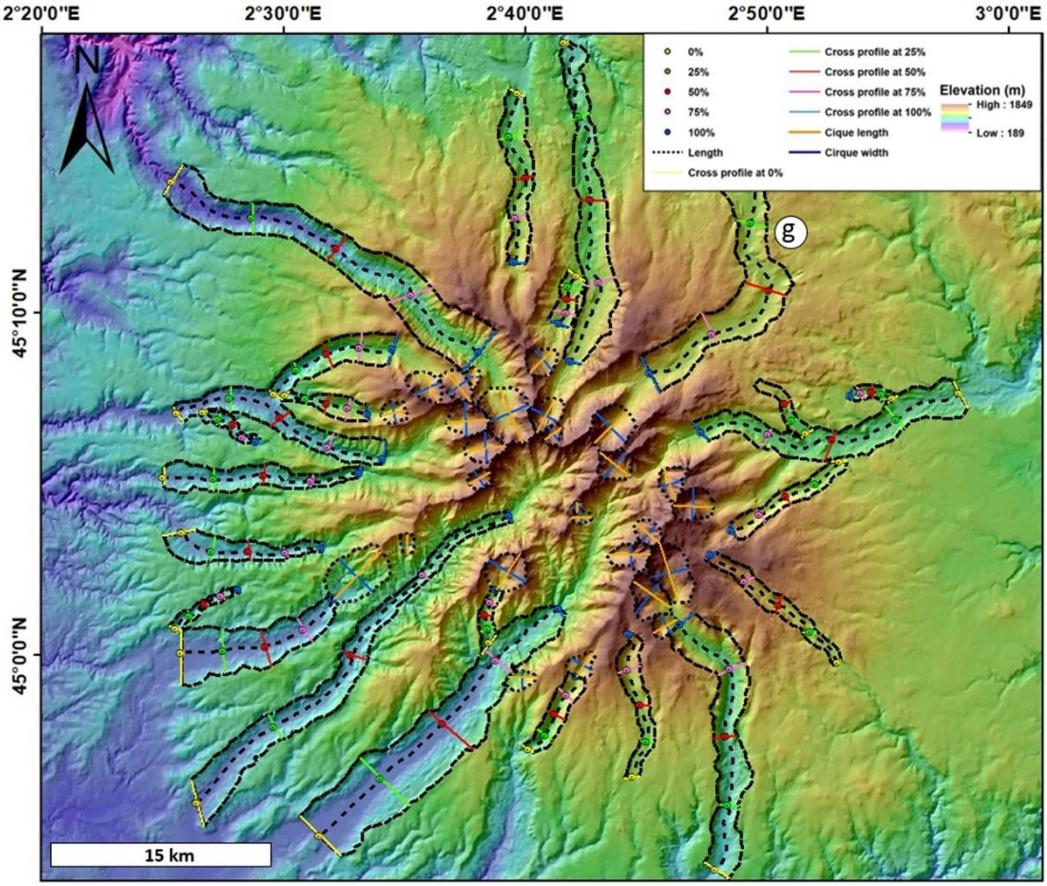

Figure 9: Study area in Cantal in French Massif Central on Earth. Colorized elevation data from 25m/pixel DEM. The white circle is the valley represented in the Fig.11 Images credit IGN.

4.4 Summary of measured parameters

The morphometric measurement allowed us to characterized 183 valleys. 36 fluvial valleys from Bakhuysen crater, 42 glacial valleys from Dawes crater (Bouquety et al., 2019), 24 glacial valleys from Cantal and a suite of valleys with unknown origin namely 12 from crater 2, 13 from crater 3, 9 from crater 4 and 47 radiating valleys. The built database, with more than 5850 usable measurements, allowed us to explore whether the valleys from crater 2, crater 3, crater 4 and the radiating valleys are more similar to fluvial or glacial valleys. The frequency distribution and the average values for each parameter and each location is plotted in Fig. 10 and in table 2. A representative cross-sectional profile for each valley population is shown in Fig.11.

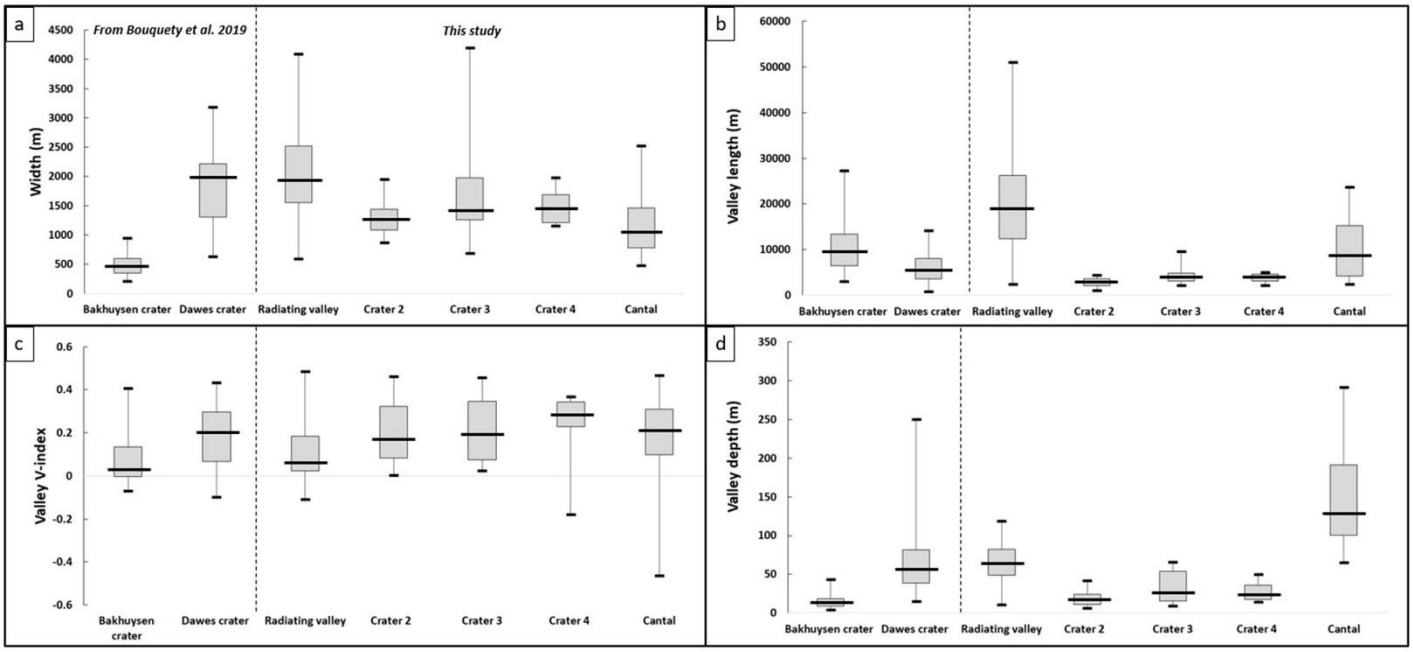

Figure 10: Box and whisker plot of valley (a) width, (b) length, (c) V-index and (d) depth. The short black lines represents the maximum and minimum for each dataset. The box represent the interquartile range, with Q1 and Q3 the bottom and top of the box. The median is represented by the long black lines in the boxes.

	Bakhuysen crater	Dawes crater	Crater 2	Crater 3	Crater 4	Radiating valley	Cantal
Number of valleys identified	36	42	12	13	9	47	24
Average length (km)	10	4.4	3	4	3.9	21	9.9
Average width (km)	0.5	2	1.3	1.7	1.5	2	1.2
Average aspect ratio length:width	21.5	2.4	2.39	2.66	2.66	10.5	8.6
Average elevation (m)	170	1600	1891	2461	2831	2594	924
Average depth (m)	15	56	18	32	27	66	167
Average cross-sectional area (m^2)	6537	24568	11111	28209	22274	147734	129937
Average V-index	0.07	0.20	0.20	0.21	0.23	0.11	0.19

Table 2: Average values for each measured parameter for valleys in each studied zone.

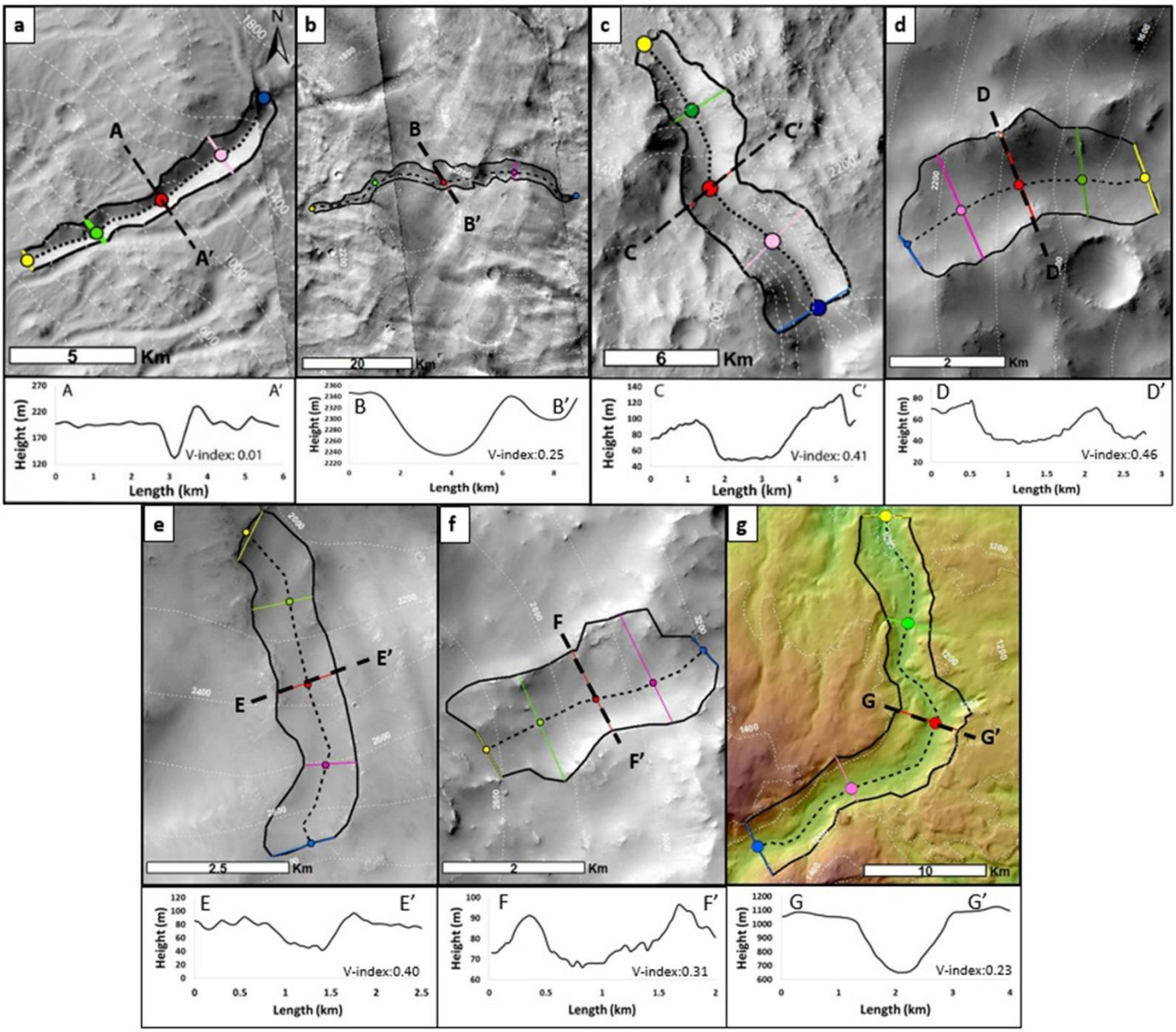

Figure 11: Examples of studied valleys and their associated V-index. The dashed line shows the cross-section at 50% of the downstream valley length extracted from HRSC and MOLA elevation data. Valley examples from (a) Bakhuysen crater (HRSC), (b) Radiating valley (MOLA), (c) Dawes crater (HRSC), (d) Crater 2 (MOLA), (e) Crater 3 (MOLA), (f) Crater 4 (MOLA) and (g) Cantal (IGN). Images credit NASA/JPL/University of Arizona.

4.5 Age estimation

To estimate the age of the valleys, we performed a crater counting analysis by measuring the crater size-frequency distribution using CTX images (Hartmann and Neukum, 2001, Ivanov, 2001). We used the method described in (Bouquety et al., 2019), which is to determine the age of the crater inner walls, where the valleys are, and the age of the crater floor fill which partially overlaps the base of the crater wall. So, estimating the age of the crater floor and the craters' inner walls allowed us to bracket the maximum and minimum age of the valleys. We measured all impact craters > 1 km, except secondary and ghost crater using CraterTools in ArcGIS (Kneissl et al., 2011) and the crater size-frequency distribution was plotted with Craterstats 2.1 software using a cumulative plot and using the function chronology from Hartmann and

Neukum (2001) and Michael (2013). Moreover, in order to constrain the period of valley formation, we used the N(1) method, based on established crater density boundaries (Bouley and Craddock, 2014). N(1) is the density of craters with a diameter >1 km normalized to an area of 10 6 km². The number of craters >1 km for each study area, associated surface areas and the N(1) are presented in Table 3 and the crater distribution map is in the supplementary (Fig. 25). In order to limit the uncertainties in age estimation arising from the small number of counted crater (Warner et al., 2015), especially in crater 2, we combined several types of datation such as the N(1) and the crater counting with function chronology from Hartmann and Neukum (2001) and Michael (2013).

	Crater > 1 km	Area (km²)	N(1)
Crater 2	6	1764	3401
Crater 3	31	5751	5390
Crater 4	20	4511	4434
Plateau	33	6056	5449

Table 3: Crater size-frequency distribution with associated area and N(1) by study area.

5 Results

5.1 Morphometric comparison: length to width ratio

Our morphometrical analysis of valley length and width allowed us to distinguish 3 groups (Fig. 12).The first one is composed of the fluvial valleys from Bakhuysen crater, they are significantly longer than they are wide with a mean aspect ratio of 22.7. The second group is composed of glacial valleys from Dawes crater and valleys from crater 2, 3 and 4. They are slightly longer than they are wide with a mean aspect ratio of 2.64 for Dawes crater, 2.39 for crater 2, and 2.66 for crater 3 and 4. Finally, the third group comprises the glacial valleys from the Cantal and the radiating valleys. The valleys from Cantal have a mean aspect ratio of 8.68 with a mean length of 9 km and a mean width of 1 km. The radiating valleys have a mean aspect ratio of 10.47. They are wide and long, about 1.9 km and 19 km in average respectively.
In order to verify if the data are statistically different, we realized a statistical test. The seven populations of valleys from the different craters are not normally distributed so we chose to use the Mann-Whitney U test. This method is used to test whether two samples are likely to derive from the same population. This nonparametric test is applicable when the samples are small ($N < 50$), not normally distributed and independent which is the case for this study. To achieve this, the first step was to rank the length/width values to obtain the critical U value and compare it with the values in Mann-Whitney table for a given N (Table 7 in the supplementary). To give an example, let compare the two populations of valleys from Bakhuysen crater (N=35) and Crater 3 (N = 13). After ranking, we obtained a critical U value of 1. For these populations, the U value in the table is 117. The critical U value from our data is strictly inferior than the U given in the Mann- Whitney table. So we can confirm that the valleys from Bakhuysen crater and Crater 3 are statistically separated, that mean that the length/width values for these two populations of valley do not follow the same trend. In other words, the erosion processes between these two populations of valleys are not the same. We realized this test between all the populations and give the result in table 4.

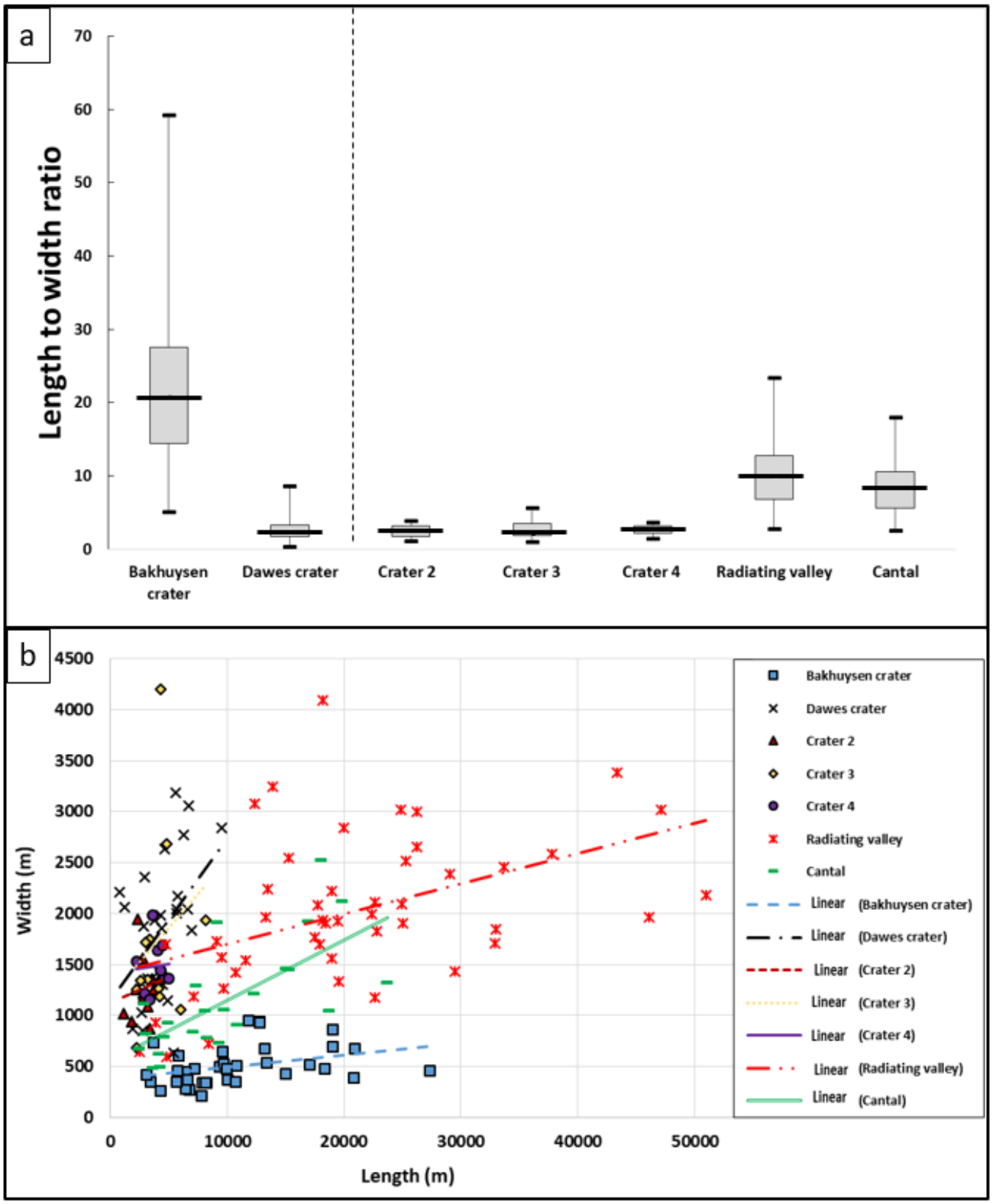

Figure 12: (a) Box and whisker plot of length to width ratio for valleys in each study areas. (b) Length versus width for all the valleys from the different study areas. 183 valleys have been plotted, 36 fluvial valleys from Bakhuysen crater, 42 glacial valleys from Dawes crater, 24 glacial valleys from Cantal and a suite of valleys with unknown origin namely 12 from crater 2, 13 from crater 3, 9 from crater 4 and 47 radiating valleys.

Valleys from:	Bakhuysen	Dawes	Crater 2	Crater 3	Crater 4	Radiating	Cantal
Bakhuysen	X	0	0	0	0	0	0
Dawes	0	X	1	1	1	0	0
Crater 2	0	1	X	1	1	0	0
Crater 3	0	1	1	X	1	0	0
Crater 4	0	1	1	1	X	0	0
Radiating	0	0	0	0	0	X	1
Cantal	0	0	0	0	0	1	X

Table 4: Result of the Mann-Whitney U test. We made the statistical analysis between all the valleys population from the different area. If the result of this test is the populations are statistically separated we put "0" and when the populations are not statistically separated we put "1". The result "1" indicates that the two studied populations follow the same trend so the erosion process between these two populations of valleys is the same. If the result is "0" it is not.

5.2 Morphometric comparison: cross-sectional area to drainage area ratio

Based on the ratio cross-sectional area to drainage area ratio, we can distinguish three groups (Fig. 13).The first one is composed of Bakhuysen crater valleys with median value of 0.0007. The second group is composed of the valleys from Dawes crater, crater 2, 3, 4 and the radiating valleys. The average median value of the ratio cross-sectional area/ drainage area is 0.0027, that is 3.8 times higher than Bakhuysen ratio. On Earth, a value of four is characteristic between glacial and fluvial valleys (Montgomery, 2002). In a previous study, we found the same ratio, around 4, between martian glacial valleys and fluvial Bakhuysen valleys on Mars (Bouquety et al., 2019). The last group is composed of valleys from the Cantal which have a ratio cross-sectional area/drainage area significantly higher than the two other groups.

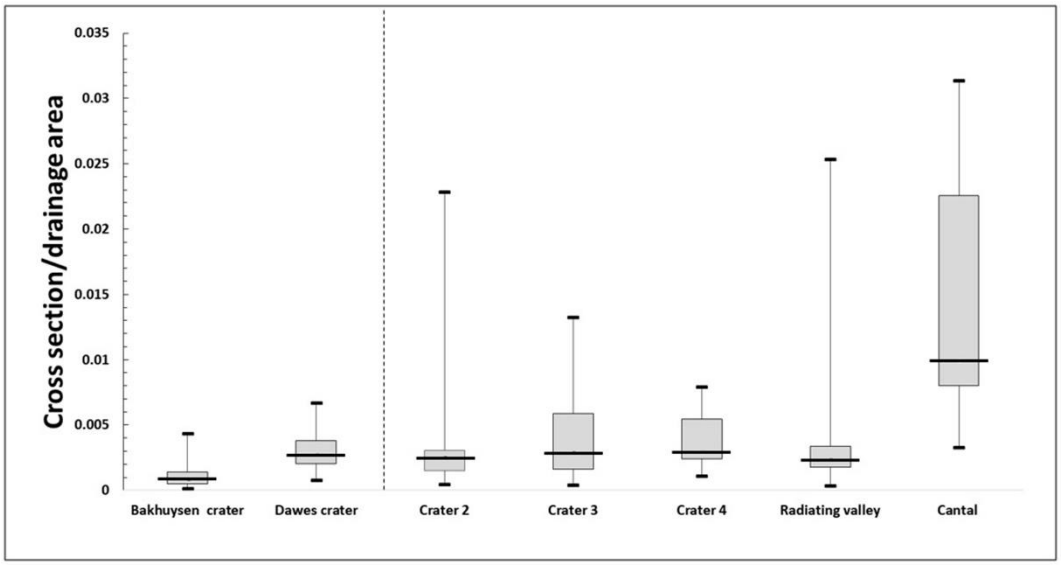

Figure 13: Box and whisker plot of cross-sectional area/ drainage area for the studied valleys.

5.3 Morphometric comparison: V-index

We studied the evolution of the cross-sectional profiles downstream from one valley in each group defined before, each chosen valley is the most representative example of their group (i.e. with a median value of parameters; Fig.14).Generally: (1) the fluvial valleys from Bakhuysen crater have a V-shape with a narrow floor and a V-index < 0.1. Their V-index is relatively constant from upstream to downstream (Fig.14a). (2) The glacial valleys from Dawes crater present a U-shape with a wide flat floor and a V-index > 0.2. Their V-index is relatively constant from upstream to downstream (Fig.14b). (3) The valleys from crater 2, 3 and 4 are U-shaped with a wide flat floor around 1.5 km and a V-index > 0.2. Their V-index is relatively constant from upstream to downstream (Fig.14c-e). (4) The radiating valleys present both V-shaped and U-shaped profiles. In fact the majority of the valleys are U-shaped upstream, and become V-shaped downstream. Upstream (i.e. > 50% of the valley length) the mean V-index is > 0.2, downstream (i.e. < 50% of the valley length) the mean V-index is ≤ 0.1 (Fig.14f). (5) Finally, the glacial valleys from the Cantal have U-shaped profiles upstream with a mean V-index > 0.2 and more V-shaped profiles downstream with a mean V-index < 0.1 (Fig.14g).

5.4 Elevation

The analysis of the elevation of the valleys allowed us to differentiate two groups. The first group, comprises valleys from Bakhuysen, they are found at an elevation <1000 m, 168 m on average (Fig. 15; Table. 2). The second group is made up of valleys from Dawes crater, crater 2, 3, 4 and the radiating valleys, they are located at an elevation higher than 1000 m with an average of 2275 m (Fig. 15; Table 2). These valleys are at an elevation 14 times higher than the valleys in Bakhuysen crater and consistent with the 1000 m of ice deposition following climate models (Wordsworth et al., 2013, Bouley et al., 2016).

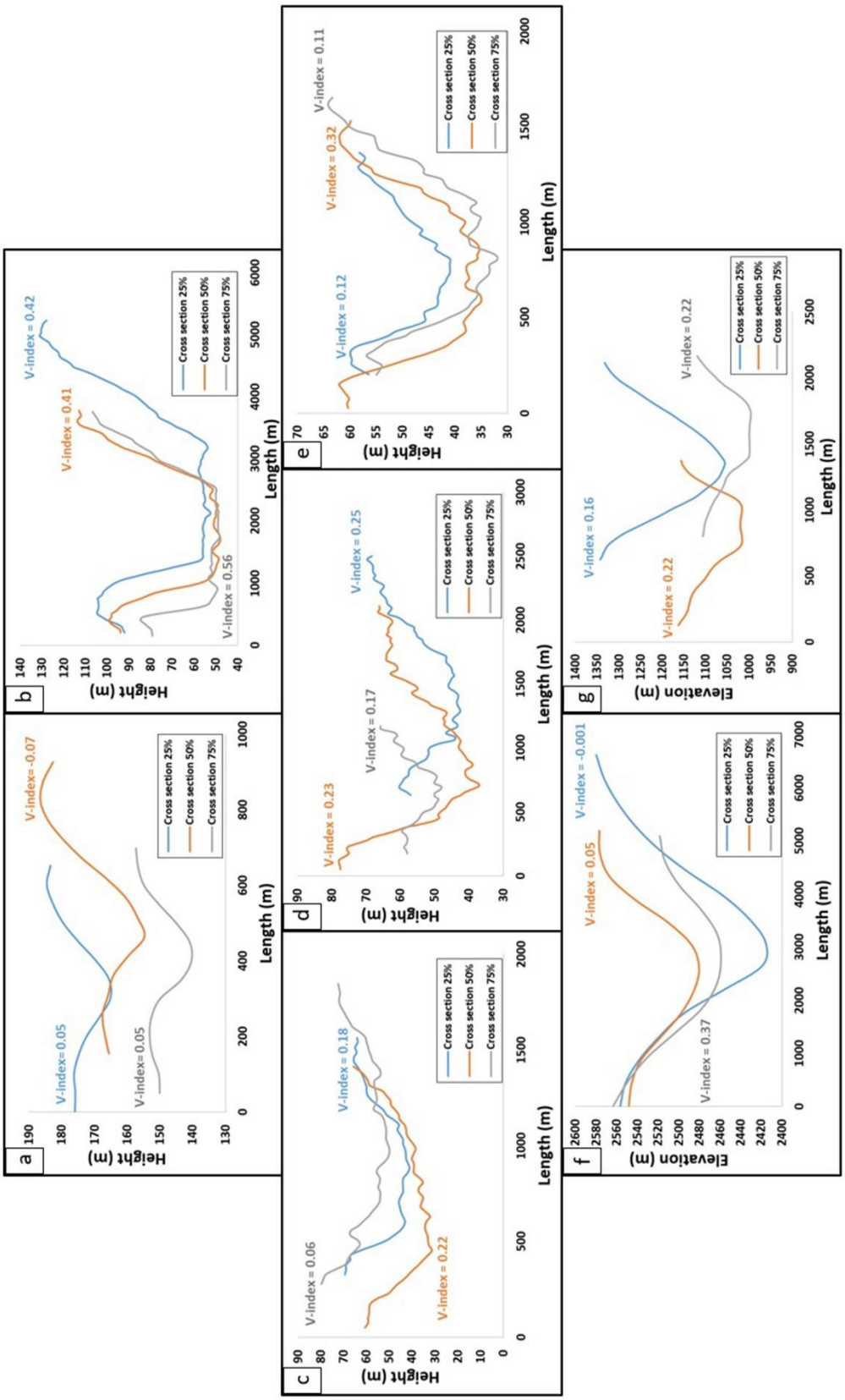

Figure 14: Cross-sectional evolution from 75% (upstream) to 25% of the valley length (downstream) and associated V-index from one representative valley for each study area. (a) Bakhuysen crater, (b) Dawes crater, (c) Crater 2, (d) Crater 3, (e) Crater 4, (f) Radiating valley and (g) Cantal. The profiles have been extracted from MOLA (c, d, e, and f), HRSC (a, b) elevation data and 25 m/pixel DEM from IGN (g).

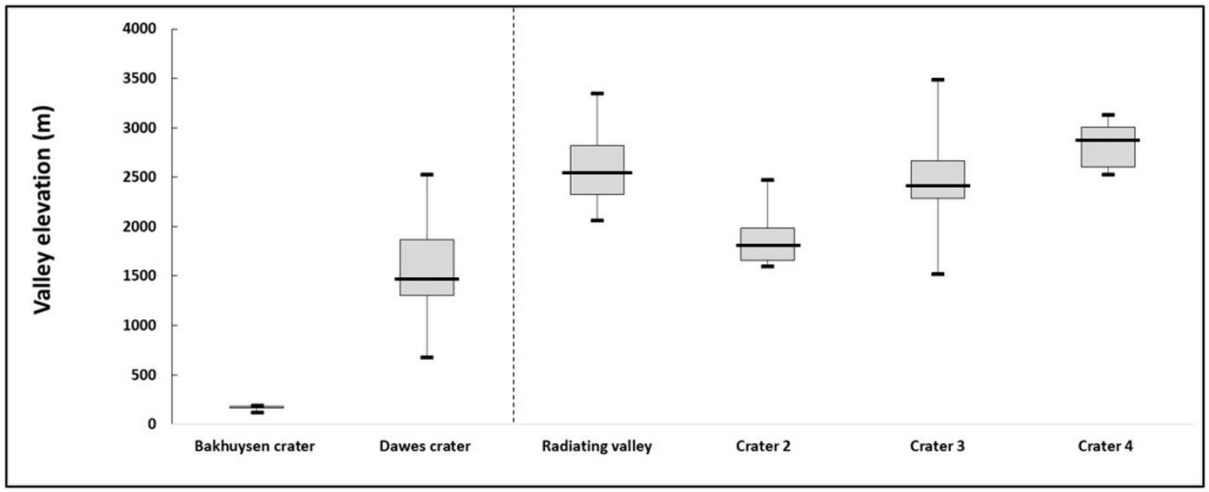

Figure 15: Box and whisker plot of elevation of the identified valleys from MOLA elevation data.

6 An interpreted glacial landscape

6.1 Glacial crater valleys from crater 2, crater 3 and crater 4

The morphometric analysis revealed that the valleys from crater 2, crater 3 and crater 4 have similar properties and trends to terrestrial and martian glacial valleys (Bouquety et al., 2019, Hobbs et al., 2016). In fact, they have a length to width ratio > 1, which is more similar to Dawes crater glacial valleys than to Bakhuysen fluvial valleys which have a length to width ratio >> 1 (Fig. 12). Long and narrow valleys are formed by fluvial processes and have an aspect ratio >>1 while short valleys are generally formed by glacial erosion with an aspect ratio >1 (Hobbs et al., 2016). Short valleys have a ratio cross-sectional areas four times larger than Bakhuysen fluvial valleys and similar to the cross-sectional area ratio of Dawes glacial valleys (Fig. 13).They are U-shaped (Fig.14c-e) with a V-index around 0.21 which is similar to the V-index found for Dawes (0.20), as well as the Cantal glacial valleys (0.19) and glacial valleys from Chamonix in the French Alps (0.21; (Bouquety et al., 2019)). This V-index value is higher than the value found for Bakhuysen fluvial valleys (0.07). Finally, the valleys from crater 2, crater 3 and crater 4 are at an elevation around 2275 m which is similar to the elevation of Dawes crater, Crater 1 and Mountain 1 (Bouquety et al., 2019). This elevation is 14 times higher than Bakhuysen fluvial valleys (Fig. 15). Moreover, the statistical distribution of the valleys from Dawes crater, crater 2, 3, and 4 are not statistically separated which indicate that the erosion process between these populations of valleys is the same (Table 4). Therefore, we interpret the valleys present on the inner walls in crater 2, 3 and 4 as glacial valleys.

6.2 Radiating valleys from the plateau

The radiating valleys present the morphological characteristics of glacial valleys described before (section 6.1). In fact, they are mainly U-shaped with a wide flat floor of 2 km, their cross-sectional area to drainage area ratio is similar to the ratio from the other martian glacial valleys (Fig. 13). Moreover, their elevation is the same as the elevation of the other interpreted glacial valleys (Fig. 15).So, we can also interpret them as glacial valleys. Nevertheless, one point differs from the characteristics of glacial valleys. The radiating valleys are much longer than the glacial crater valleys (Fig. 10b; Fig. 12). This difference could be explained by the fact that the radiating valleys are not limited by the short steep slope of the crater inner walls as the other studied valleys, but they extend over tens of kilometres on the gentle slope of the plateau. The distribution described by the length to width ratio of the radiating valleys is between the fluvial

trend described by Bakhuysen valleys and the glacial trend described by glacial valleys in the different craters (Fig.12 b; (Hobbs et al., 2016, Bouquety et al., 2019)) and is similar with the valleys from the Cantal. The Mann-Whitney U test for the Cantal and the radiating valleys are not statistically separated which indicate that the erosion process between these two populations of valleys is the same. Furthermore, the valleys from the Cantal and the radiating valleys are statistically separated from the valleys from Dawes, crater 2, 3, and 4 which indicates that they have a different origin or other processes have intervened in their formation (Table 4). Moreover, the radiating valleys become more V-shaped downstream around the cross-section 25% of the valley length, just as the glacial valleys from the Cantal which have been shaped by several phases of glaciation and melting (Fig. 14f-g; (Boule, 1896, Durand, 1939, Veyret, 1973, Valadas and Veyret, 1981)). All these properties seem to indicate that the radiating valleys are mainly glacial valleys. Nevertheless, the length, the slope and the V-shape downstream of the radiating valleys seems to suggest that other processes played a role in their formation (discussed in the section 7.3).

6.3 Evidence for a plateau ice cap: comparison with the Earth

On Earth, many mountain regions contain high plateaus which may act as accumulation areas for icefields. These plateaus often have outlet glaciers which spill from higher level accumulation areas down into adjacent valleys (Rea et al., 1998), for example in the Cantal or the Shaluli Shan in the Tibetan plateau. These areas present evidence of paleoglaciation where an ice reservoir was at the origin of the valleys (Boule, 1896, Durand, 1939, Veyret, 1973, Valadas and Veyret, 1981, Derbyshire et al., 1991, Kuhle, 1998, Heyman et al., 2008, Fu et al., 2013a, Fu et al., 2018). The presence of depositional features such as moraines, kames, eskers, or kettles hole and features such as glacial lineation, scoured terrain, hummocky terrain and moraines indicate that these areas was covered by an ice cap at the highest elevation (Boule, 1896, Durand, 1939, Veyret, 1973, Valadas and Veyret, 1981, Derbyshire et al., 1991, Kuhle, 1998, Heyman et al., 2008, Fu et al., 2013a, Fu et al., 2018). Ice caps with cold-based regimes are weak agents of erosion compared to those with wet-based regimes. Their interiors commonly have lower erosion rates than their margins and outlet glaciers as a result of low ice surface slopes and lower rates of meltwater delivery to the bed (Hallet et al., 1996, Cowton et al., 2012, Fu et al., 2013a, Fu et al., 2018). But it had been demonstrated that for the Greenland ice sheet margin, the erosion rates are much higher than the average rate across the ice sheet as a whole and closely resemble to the erosion rate of alpine glacier with surface meltwater reaching the glacier bed at a distance of tens of kilometres from the terminus (Bartholomew et al., 2011, Bartholomew et al., 2011b, Cowton et al., 2012). Land-terminating outlet glaciers originate from the ice sheet margins, due to the glacier extension, the increased ice surface slope and the increased supply to meltwater to the glacier bed creating higher erosion rates. These land-terminating outlet glaciers, similar to alpine glacial valleys, are warmed-based and have basal erosion rates of about 0.1 to 10 mm/yr compared to 0.01 mm/yr for the ice sheet (Hallet et al., 1996, Koppes and Montgomery, 2009).

The study area presents 71 glacial valleys in the three craters and on the slope of the plateau (Fig.16a). We observed that the glacial crater valleys are located everywhere on the inner slopes in crater 3 and 4 without preferential distribution, contrary to glacial crater valleys in crater 2 which are located preferentially on the northeast facing wall, in contact with the plateau area (Fig.16b). The radiating glacial valleys start from the plateau at an elevation around 3000 m (Fig.16b, c). Whether in the craters inner walls or on the slopes, all the observed valleys seem to emerge from the high elevation plateau (around 3000 m) and do not present any clear valley heads and/or glacial cirques such as the glacial valleys identified in Bouquety et al., 2019 (Fig.16c).

So, we propose that the plateau was covered by an ice cap, and at the margin of this plateau, we observed the presence of glacial valleys (Fig.5e; Fig.17).This hypothesised plateau ice cap was characterized by an area of 6137 km² at an elevation of 3150 m. By analogy to several sites on Earth: Scotland (Sugden, 1968), Scandinavia (Kleman and Stroven, 1997, Stroeven et al., 2002, Fabel et al., 2002), Cantal (Boule, 1896, Durand, 1939, Veyret, 1973, Valadas and Veyret, 1981, Etlicher and Hervé, 1988), Arctic Canada (Sugden and Watts, 1977, Sugden, 1978, Briner et al., 2003)), New Zealand (Suggate, 1990) and the Tibetan Plateau (Derbyshire et al., 1991, Kuhle, 1998, Heyman et al., 2008, Fu et al., 2013a, Fu et al., 2018), we propose that the glacial landscape was characterized by an erosional polythermal regime where the highest elevations were protected by a cold-based plateau ice cap while, at the margins of this plateau and at lower-altitude warm based alpine glacial valleys flowed radially from the plateau (Fig. 17). The presence of an ancient plateau ice cap could explain: (1) the absence of glacial cirques, which means that the glacial valleys would come directly from this plateau ice cap forming outlet glacier, and (2) the preferential distribution of the glacial valleys in crater 2 which are localized only on the inner wall in contact with the plateau.

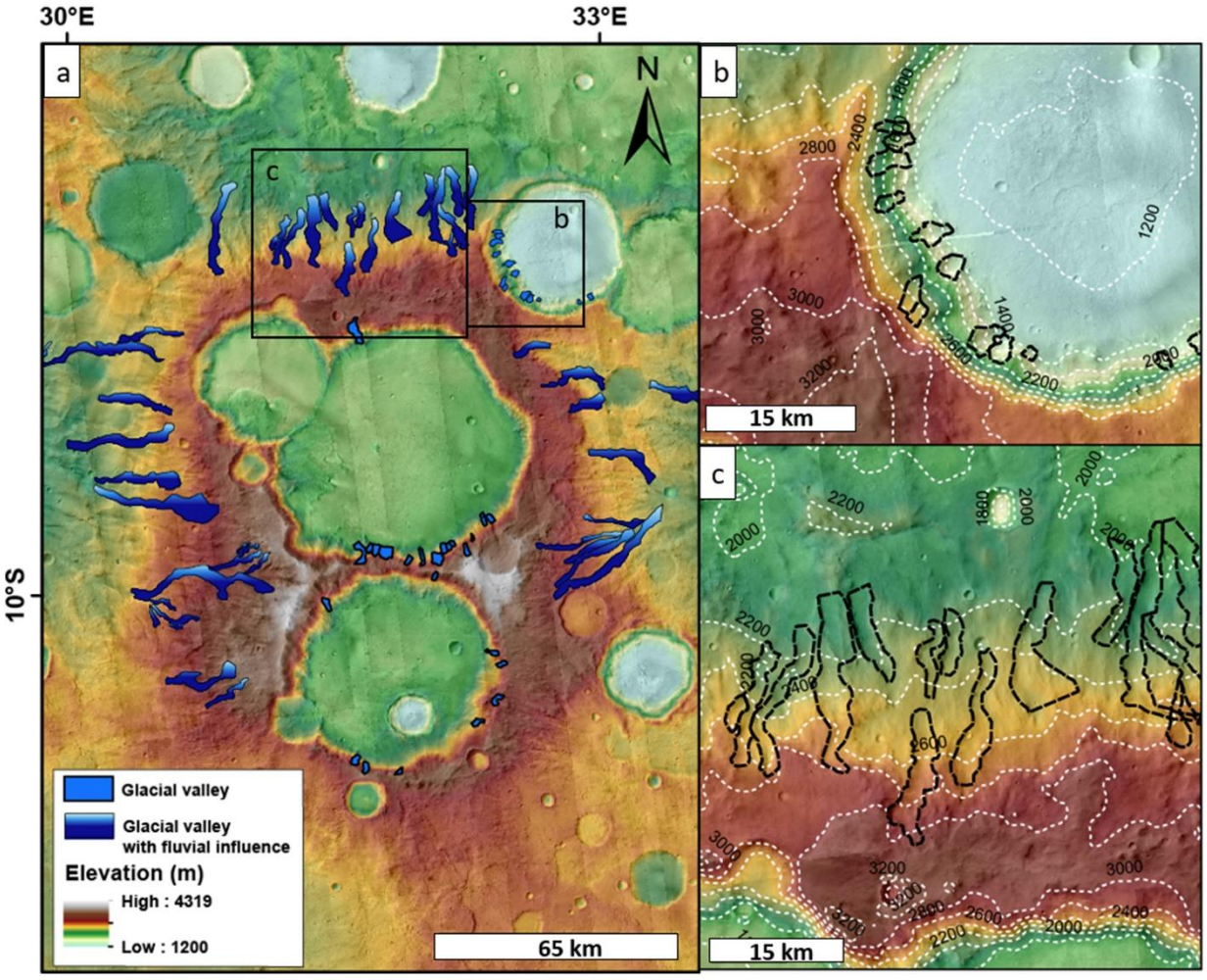

Figure 16: Interpreted glacial valleys. (a) Study area with the interpreted glacial valleys (blue polygons) with associated zoom in (b) and (c). CTX images with MOLA background. (b) Zoom on the preferential distribution of the valleys in crater 2, they are located preferentially on the northeast facing inner wall, in contact with the plateau area. (c) Zoom on the northern slope, showing that the valleys do not have any clear valley heads and/or glacial cirques. The valleys come directly from the plateau. Images credit NASA/JPL/University of Arizona.

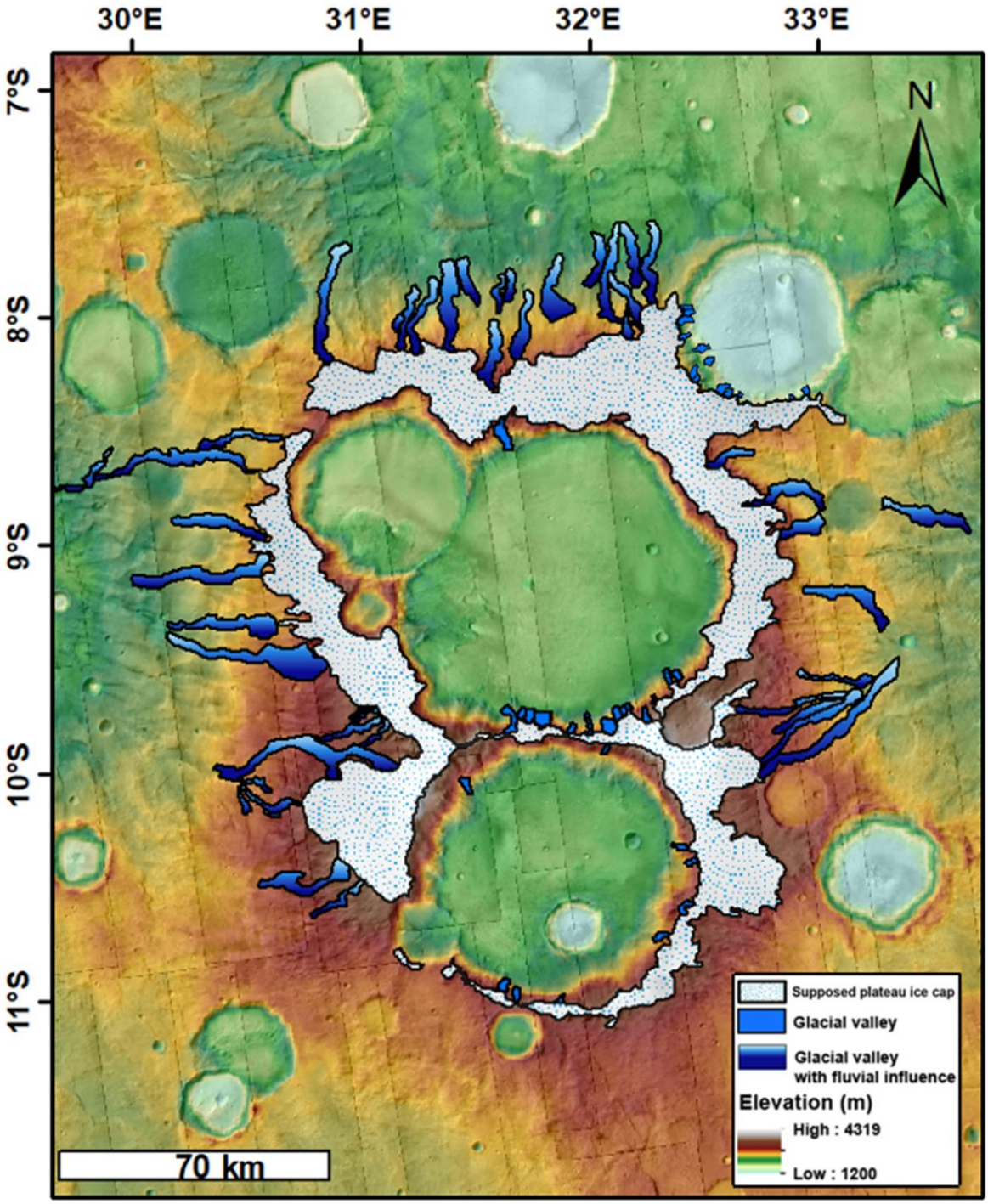

Figure 17: Geomorphological map of the proposed glacial landscape. Distribution of the glacial valleys on the inner walls of craters 2, 3 and 4, and the supposed plateau ice cap. To construct this ice cap, we extracted all the point "100%" corresponding to the valley upstream, then we connected these points together. Then to extrapolate we used the topographic data such as the slopes and the isolignes in order to localize the flat area at high elevation associated with a visual interpretation of the landscape morphology. The supposed ice cap thus drawn represents the minimum extend of the ice. CTX images with MOLA background. Images credit NASA/JPL/University of Arizona.

6.4 Timing of the formation of the glacial landscape

6.4.1 Glacial valleys

In order to bracket the age of the potential glacial valleys, we analysed the crater-size frequency distributions of the inner rim walls and the floor of crater 2, 3 and 4. The fits indicate that, in the three craters, the crater floors are younger than the crater inner walls where the valleys are, so the valleys are younger than the crater walls but older than the filling material of the crater floor that covers them (section 4.5). The crater size frequency distribution for each location is represented in the Fig.18. The results are summarized in Table 5. So, the age of the measured glacial landscape is probably between 3.31 and 3.65 Ga (Late Noachian/ Early Hesperian).

	Crater floor (Ga)		Crater wall (Ga)	
	Hartmann and Neukum, 2001	Michael, 2013	Hartmann and Neukum, 2001	Michael, 2013)
Crater 2	3.38 ± 0.30	3.31 ± 0.43	3.59 ± 0.07	3.54 ± 0.06
Crater 3	3.49 ± 0.11	3.38 ± 0.18	3.65 ± 0.7	3.60 ± 0.08
Crater 4	3.44 ± 0.15	3.37 ± 0.22	3.62 ± 0.06	3.56 ± 0.08

Table 5: Ages estimation of crater walls and floors for each areas and using two different chronology function.

The crater densities N(1) for crater 2, 3, and 4 are respectively 3401, 5390 and 4434. These crater densities correspond to the Early Hesperian for crater 2 and Late Noachian/Early Hesperian for craters 3 and 4 according to the established crater density boundaries (Tanaka, 1986, Hartmann, 2005). These ages are also consistent with the age found by Bouley and Craddock, 2014 with the basin age-dating method for the basins and subbasins within Terra Sabaea of 3.61 ± 0.02 Ga.

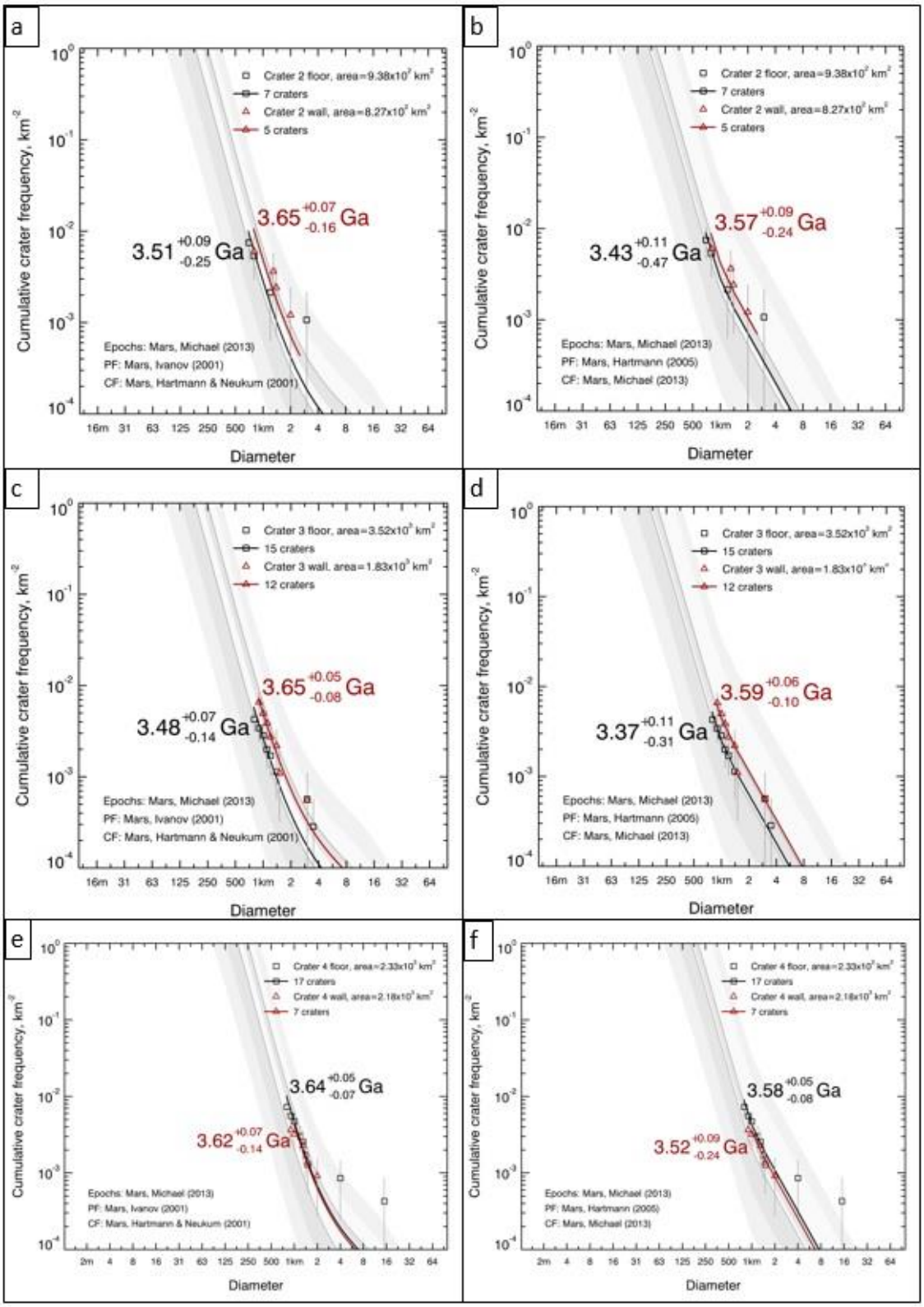

Figure 18: Age estimations of the glacial landscape. The red triangles represent the counts performed on the inner wall and the black squares the counts performed on the crater floor. Crater 2: crater-size frequency distribution for crater >1km with (a) Hartmann and Neukum (2001) chronology function and (b) Michael (2013) chronology function. Crater 3: crater-size frequency distribution for crater >1km with (c) Hartmann and Neukum (2001) and (d) Michael (2013). Crater 4: crater-size frequency distribution for crater >1km with (e) Hartmann and Neukum (2001) and (f) Michael (2013). A detailed map of the count area is in the supplementary (Fig.25).

6.4.2 Plateau ice cap

In order to date the supposed plateau ice cap (previously defined in Fig. 17), we analysed the crater-size frequency distribution (>1km) in that area (Fig.25g in the supplementary, table 3). The crater size-frequency distribution, for craters diameters <3km gives a best-fit age of 3.59 ± 0.035 Ga with Hartmann and Neukum (2001) chronology function and 3.49 ± 0.037 Ga with Hartmann (2005) chronology function (Late Noachian/Early Hesperian; Fig. 19). These ages are confirmed by a N(1) crater density of 5449 which corresponds to the Late Noachian/Early Hesperian according to the established crater density boundaries (Tanaka, 1986, Hartmann, 2005). The crater size-frequency distributions show two trends for each chronology function (Fig. 19 a,b). The first one is 3.74 ± 0.14 Ga with Hartmann and Neukum (2001) chronology function and the second is 3.59 ± 0.22 Ga with Hartmann (2005). These ages are found with the best-fit given by the three biggest craters on the plateau (>2.5km). So, we suppose that resurfacing processes occurred between 3.74 and 3.59 Ga or between 3.59 and 3.49 Ga which can explain the absence of smaller craters following the isochron of 3.74 Ga for Hartmann and Neukum (2001) and the isochron of 3.59 Ga for Hartmann (2005).

These glacial valleys and the plateau ice cap are dated at the same age than the glacial landscapes in Bouquety et al. (2019), between 3.34 and 3.66 Ga. Therefore, we hypothesize that from the Late Noachian to the Early Hesperian, the climatic conditions in Terra Sabaea were cold and humid enough for precipitation of snow and to have deposition and preservation of ice leading the formation of an ice cap and outlet glaciers.

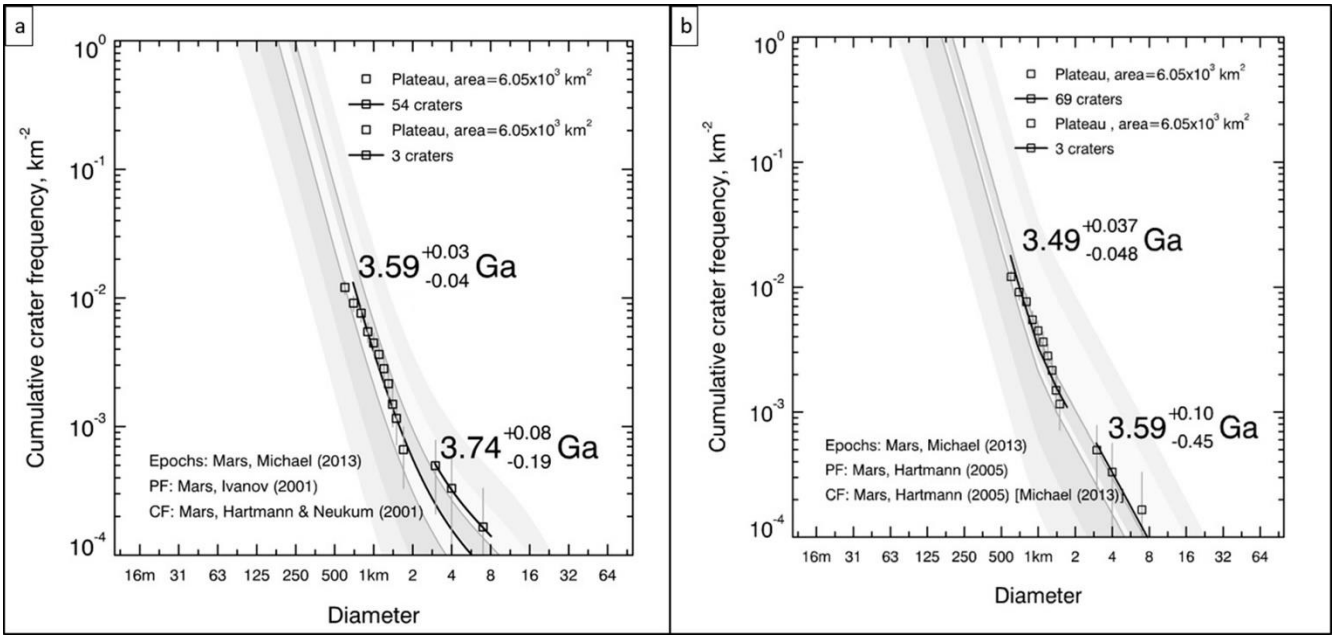

Figure 19: Timing of formation of the supposed plateau ice cap. (a) With Hartmann and Neukum (2001) and (b) with Hartmann (2005). These figures show the crater size frequency distributions > 1km, on the plateau area (a detailed map is in the supplementary). We observe in (a) that the crater size frequency distribution follow two different isochrons. The 3.59 Ga isochron is composed of the smallest crater in the plateau (<2km in diameter) and the 3.74 Ga isochron have the crater with a diameter > 2.5 km. The fact that the same crater population follow two differents isochron seems to indicate that resurfacing processes occurred between 3.74 and 3.59 Ga probably caused by the plateau ice cap.

7 Discussion

7.1 Quantification of uncertainties

The morphometrical comparative analysis we did in this study used two different types of DEM, the HRSC DEM and the MOLA DEM. The HRSC DEM was used for the valleys measurement of Bakhuysen crater and Dawes crater and the MOLA for the valleys from craters 2, 3, and 4 and the radiating valleys. Thus, it is important to quantify the uncertainties resulting from differences in resolution between the MOLA (463 m/pixel based on the MOLA laser shots) and the HRSC DEM (10-50 m/pixel). In order to do this, we compared the cross-sectional profiles extracted from the MOLA and the HRSC DEM for the same location (Fig.20a). The difference in the number of data point on the line (217 for HRSC and only 16 for MOLA) make the MOLA profiles smoother than the HRSC ones which is more precise with more variations (Fig.20b). Moreover, the shape of the two profiles are different. The HRSC profiles looks more V-shaped than the MOLA ones and they are shifted. There is a difference in the cross-sectional area and in the depth of the valley. These differences are about 8% for the cross-sectional area and 13% for the depth (Fig.20c). But, in this study, the cross-sectional area and the depth are never used as singles ones parameters. Indeed, the cross-sectional area is used to calculate the cross-sectional/drainage area ratio, and the depth to calculate the V-index. (1) The cross-sectional/drainage area ratio is calculated by dividing the cross-sectional area with an order of magnitude of 10 5 m² by the drainage area with an order of magnitude of 10 8 m² (extracted from the mean values). So, this difference of order of magnitude make the uncertainty of the cross-sectional area negligible. (2) The depth is used to calculate the V-index. Between the two DEM, for a same profile, the mean V-index difference is around 0.05. This difference can induce bias in the interpretation of small V-index (<0.1) than bigger ones (>0.2). In fact, the mean V-index for the valleys from Bakhuysen crater is 0.07, thus ± 0.05 can false the interpretation. A section with a V-index= 0.02 will be interpreted as fluvial but the same section with a V-index= 0.13 will be interpreted as glacial. The mean V-index for Dawes valleys is 0.20, ± 0.05 on this values still make the interpretation as glacial valleys. But, this analysis does not depend on the value of a single parameter, it depend of the comparison of several parameters. So, even if the interpretation about the V-index could be changed by the uncertainties, the analysis of the other parameters allows to circumvent this problem. The other parameters used like the length, the width and the drainage area, are only dependent on the projection used. We extracted these values using the “SimpleCylindrical_Mars” projection. With this projection, distortion increases as the distance from the standard parallels increases. Our study areas are near the equator (between 2° and 9°S), which is a standard parallel so the distortions can be neglected. The valleys from craters 2, 3, and 4 and the radiating valleys have been studied using MOLA DEM only because there is no HRSC data available in these areas (Fig.24 in the supplementary). So the uncertainties can only come from the resolution of this dataset. We can not use the MOLA laser shot because the orbit of the MOLA instrument is not consistent with the measurements by section required for this study. The uncertainties in this analysis are important to considerer because it can false the interpretation about the origin of the valleys. But the number of measured parameters allows to compare the data and reduce the uncertainties.

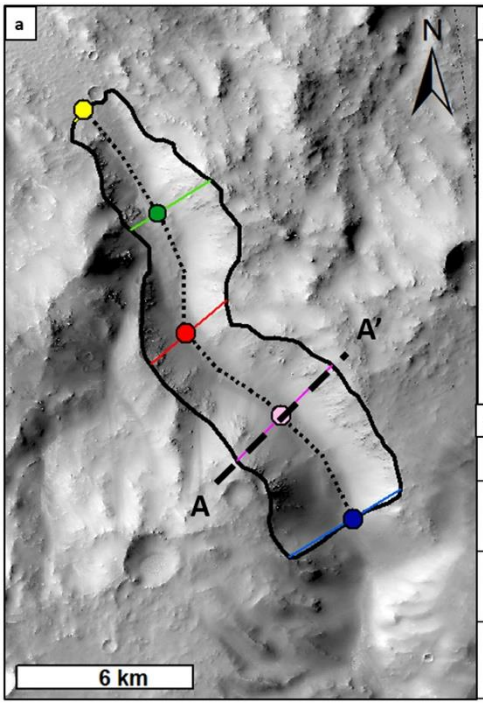

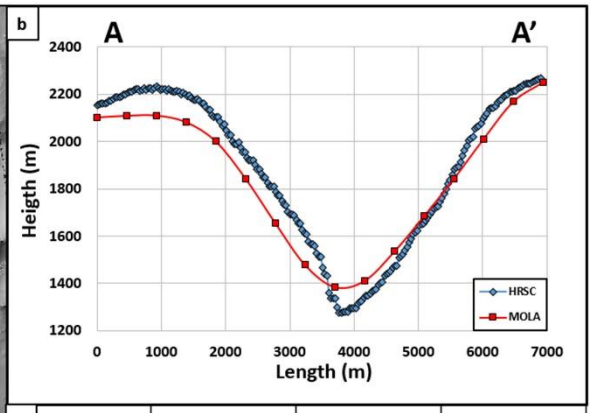

c

	Cross-section (m²)	Depth (m)	V-index
MOLA	1966259	724	0.07
HRSC	1811451	836	0.02
Uncertainty	±154807 (7.8%)	± 112 (13.5%)	± 0.05

Figure 20: Quantification of uncertainties. (a) CTX image of a valley in Dawes crater. The dotted line is the profile shown in (b). (b) Cross-sectional profiles from MOLA in blue and HRSC DEM in red. (c) Table of values from the selected parameters. Images credit NASA/JPL/University of Arizona.

7.2 Estimation of the elevation line altitude: ELA

The glacial landscape in the study area is today totally ice free making the identification and the characterization of glacial properties complicated. However, Anderson et al. (2006) developed a geometrical protocol in order to estimate the elevation line altitude (ELA) in glacial valleys on Earth. This method is a study of the geometrical properties of a glacial valley, such as the distance down-valley (valley length), the elevation and the linear profiles of the valley bed and valley rim (Anderson et al., 2006). Several assumptions are needed: (1) the initial profile is linear, (2) the width of the valley is uniform, (3) the annual mass balance varies linearly with elevation, (4) the glacier at any time is quasi-steady, (5) the erosion rate is proportional to ice discharge per unit valley width, and (6) glacial erosion rates far exceed fluvial erosion rate (Anderson et al., 2006). The distribution of ELA predicts erosion peaks at 30–40% of the down-valley distance to the glacial limit, and the pattern merges smoothly with the steeper fluvial profile downstream of the glacial limit (Anderson et al., 2006).

Even if we do not have information about the martian annual mass balance and the glacial erosion rates, we decided to apply this method to a valley in our study area (Fig.21). In order to estimate the ELA in this valley, several steps are necessary: (1) extract the profile of the valley bed and the valley rim and extract the linear equation of the valley bed. (2) Plot the valleys rim and bed profiles using the equation for the valley bed making it linear to follow the assumption (1) described by Anderson et al. (2006), (Fig. 21a). (3) Then we calculated the Xela which is the position of the ELA following the length of the valley, we estimated the Xela at 1/3 of the valley length (Anderson et al., 2006). (4) We calculated the Zela following: Zela=(-Xela*S) +Zmax with Zela the elevation of the ELA, S the slope and Zmax the maximum elevation of the valley (Fig. 21a). (5) Finally we calculated the terminus position of the supposed glacier, Xterm: Xterm=2* Zmax-Zela S. This method allowed us to estimate the ELA at 2556 m, the other values obtained with this method are sum up in the table 6.

In order to verify this geometric approach, we reported the values obtained on the studied valley (Fig. 21b). In a geomorphological approach, we observed that before the Xela point (green

square, Fig. 21b) the valley presents a circular-like form with non-parallel rims. Below this point, the rims become sub-parallel until the Xterm point (yellow square, Fig.21b). The morphology of the valley is consistent with the points obtained by the geometrical analysis. In fact when X < Xela, it is the accumulation zone, which often results in a hollow form in glacial landscape. Then, when X > Xela it is the ablation zone, where the erosive power of the ice is more effective. The glacier erosion made U-shaped valleys with parallel steep rims and a flat floor (Fig.21c). When X ≥ Xterm, where the supposed glacier terminated, we do not observe well-marked rims with high elevation but it is still possible to follow the valley downstream (Fig. 21d). Moreover, we can discuss about the evolution of the rim longitudinal profile. Above the ELA, the rim is well marked with a mean elevation of 100 m above the valley bed. Below the ELA, the rim is much smaller with a mean elevation of 15 m above the valley bed. Finally, the X term point is consistent with the results of the morphometrical analysis. In fact we observed that the radiating valleys become more V-shaped at 25% of the valley length (described in section 6.2). Upstream, the valley are U-shaped with a V-index > 0.1 shaped by the glacial erosion (Fig.21e). After the 25%, downstream at the maximum extend of the glacier (X term), the glacier could have melted allowing the liquid water to shape the V-shaped valley downstream with a smaller V-index (Fig.21f).

We can discuss about the uncertainty of this method. This geometric method is highly based on the valley length. On Mars, especially on Terra Sabaea, the valleys are often degraded and it is complicated to follow the rims making the interpretation of the valley length complicated. We chose to study this valley with this method because it is relatively well preserved and we can follow the rim from the plateau area upstream to the lowest elevation downstream. Moreover, the assumptions made, and the absence of information about the martian annual mass balance and the glacial erosion rates can changed the interpretation. Nevertheless, the fact that the morphology is consistent with the geometry is a good indicator that shows that Terra Sabaea have been icy at elevations higher than 2556 m 3.6 Ga ago.

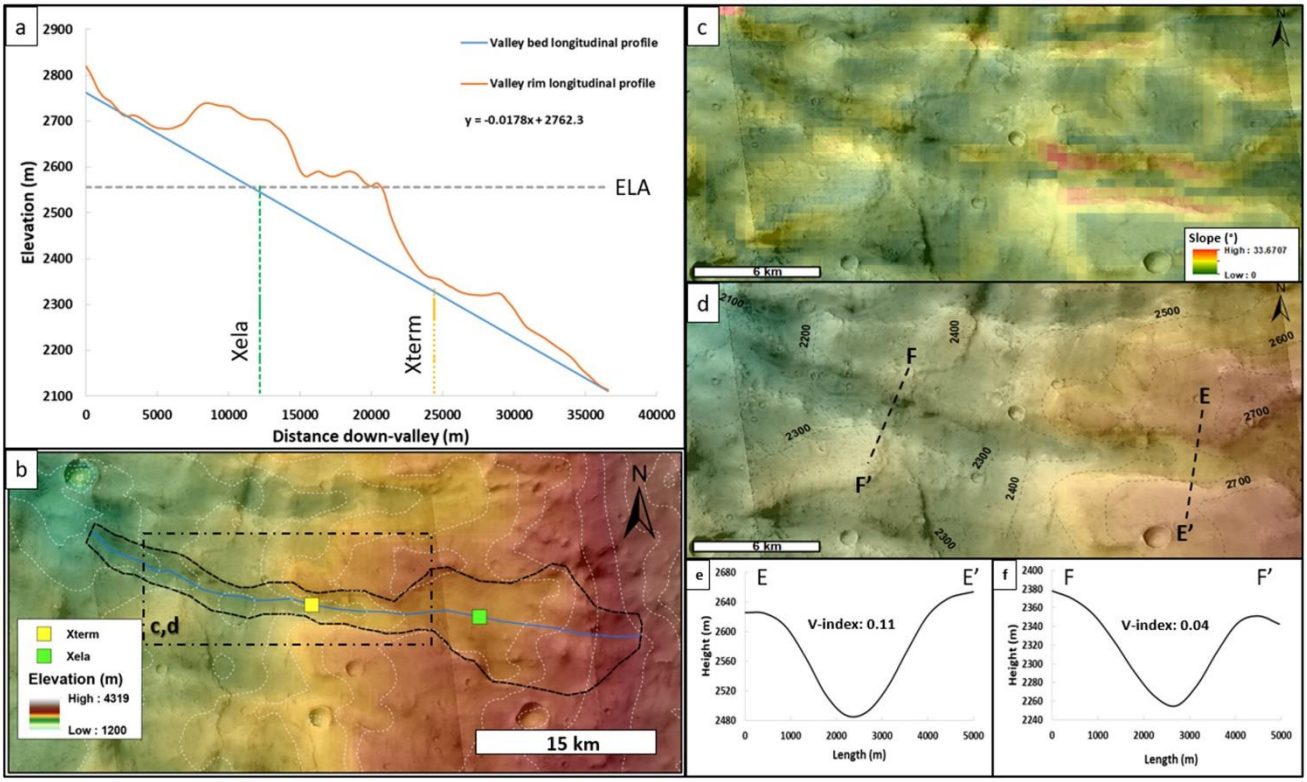

Figure 21: Estimation of the elevation line altitude (ELA) by a geometric approach following the method described in Anderson et al. (2006). (a) Longitudinal profile of the valley (on western slope of

the plateau area). The blue and orange lines represent the linear profile, respectively, of the valley bed and the valley rim. Xela is the position of the ELA following the valley length and Xterm is the glacier terminus position. (b) Studied valley for the ELA estimation. The yellow and green squares represent respectively the Xterm and the Xela. The blue line is the valley length used to construct the linear valley bed profile show in (a). The dotted rectangle is the area zoomed in (c) and (d). (c) Slope map of the zoomed area calculated from MOLA. (d) MOLA elevation map of the zoomed area. The dotted lines are the topographic profiles showed in (e) and (f). (e) Cross-sectional profile from MOLA with associated V-index. (f) Cross-sectional profile from MOLA with associated V-index. CTX images with MOLA background. Images credit NASA/JPL/University of Arizona.

Distance (m)	Zmax (m)	Zmin (m)	Slope	X term (m)	X ela (m)	Z ela (m)	Function of the valley bed
36573	2773	2108	0.0178	24382	12191	2556	y= -0.0178x + 2762.3

Table 6: Calculated parameters using the method from by (Anderson et al., 2006)

7.3 Comparison with the Tibetan plateau

The area of Shaluli Shan, in the southeastern Tibetan Plateau (30°44'N, 99°44'E), presents evidence for past polythermal ice cap glaciation (Fu et al., 2012, Fu et al., 2013a). This area is strongly shaped by present and ancient glacial processes from the last glaciation (Fig. 22 a-c). Shaluli Shan is composed of ice-free wide (20 km) plateau at high elevation (4200 m), many alpine glacial valleys extend downslope from this plateau (Fig. 22c, (Fu et al., 2013a)). These alpine glacial valleys have lengths up to 45 km, have an average width of 3 km and are deeply incised (between 100 to 400 m) into the slopes surrounding the plateau. These glacial valleys can merge to produce exceptionally long, more than 20 km, glacial valleys (Fu et al., 2012, Fu et al., 2013a). Although the plateau is ice-free, it is possible to observed abundant glacial landforms radiating from the plateau which is the highest area in this region. At smaller scales, it is possible to find in this area several patterns of glacial erosion and deposition: (1) lateral moraines. (2) Hummocky terrain comprises irregular shaped sedimentary deposits of hills and mounds often located along the glacial valley sides (Bennett and Glasser, 2011). (3) Glacial lineations are elongated features formed by subglacial streamlining, including both erosional and depositional processes (Hargitai and Kereszturi, 2015). (4) Scoured terrain, formed by glacial plucking and abrasion, consists of low-relief bedrock-dominated surfaces with numerous rock basins and intervening rock knobs, typically resulting in a widespread occurrence of lakes (Fig. 22b; (Fu et al., 2012)).

The abundant glacial landforms in the Shaluli Shan, mark the former extent of past glaciations including plateau ice caps and extensive alpine glacial valleys. This paleoglacial landscape composed of a large plateau ice cap linked with radiating glacial valleys indicate that the ice cap was the source of the alpine glacial valley downstream (Fu et al., 2013a). Moreover, Shaluli Shan was shaped by polythermal glaciation (Fu et al., 2013a). The plateau ice cap was characterised by a cold-based thermal regime, producing small scale erosional features such as hummocky terrain or glacial lineations, while the alpine glaciers downslope were characterised by warm-based thermal regimes. (Cowton et al., 2012, Fu et al., 2013a). These two glacial systems were linked together by surface meltwaters that penetrated to the glacier bed at the ice cap margin. Meltwater is an important catalyst for enhanced glacial erosion by alpine glacier; its presence promotes high water pressures which enhance basal sliding of the glacier with associated erosion (Cowton et al., 2012). This landform assemblage is characteristic of an extensive paleoglacial landscape and is very similar to the one we studied in Terra Sabaea.

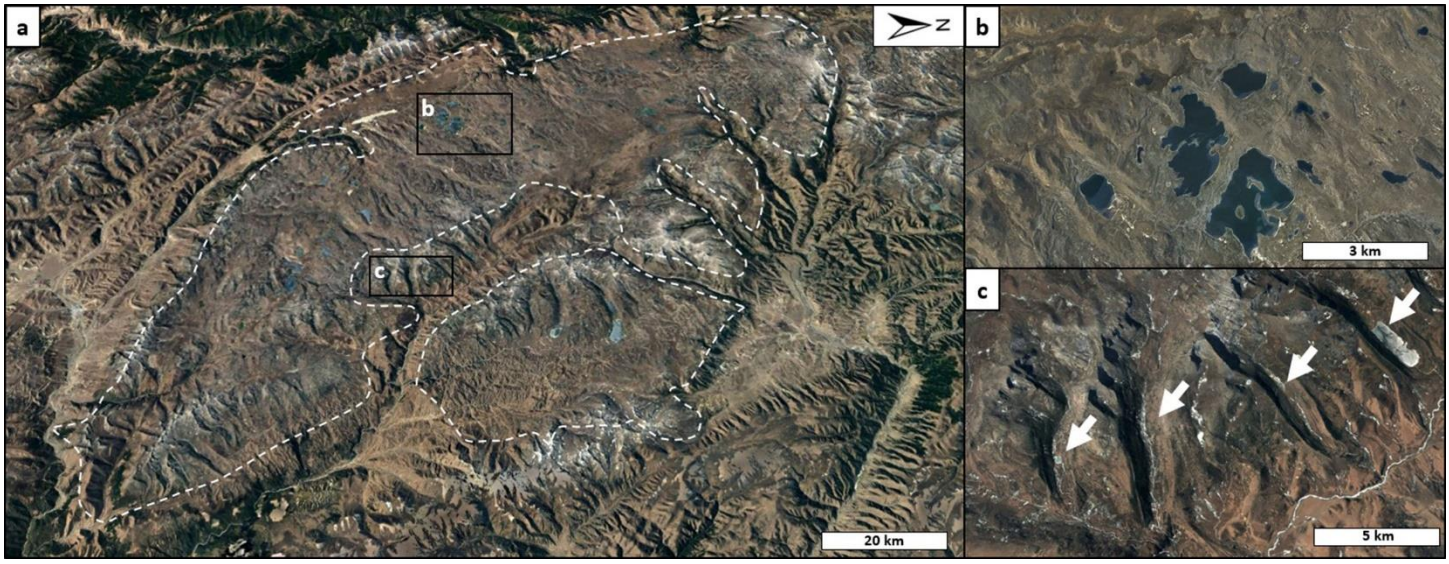

Figure 22: Satellite images of Shaluli Shan area. (a) Zoom on the Haizishan plateau. The white dots polygons show the plateau around 4200 m in elevation. (b) Zoom on scoured terrain with lakes and (c) zoom on glacial valleys originating from the plateau. The glacial valleys are shown by the white arrows. Images credit Google Earth.

7.4 Glacial landscape in Terra Sabaea: A complex system

The studied glacial morphologies in Bouquety et al. (2019) and in this study indicate that during the Late Noachian/Early Hesperian the climate was cold and wet enough to allow deposition of snow/ice and preservation of ice leading to formation of glaciers and an ice cap shaping the landscape in Terra Sabaea. We did not find any depositional features such as moraines, eskers or glacial lineations, even by analysing the two HiRISE images available in the area. Two scenarios are possible: (1) This absence could be because this depositional features are mainly composed of easily erodible unconsolidated sediment, and have been removed by subsequent erosion by wind, meteoritic impacts, run-off or covered by depositional material. (2) These depositional features could have never formed. On Earth, the Meserve Glacier in Antarctica, which is a cold-based glacier had eroded U-shaped valleys. Cuffey et al. (2000) proposed that this cold-based glacier occupied older river channels and eroded U-shaped valleys. Thus, they did not found depositional features characteristics of warmed-based glaciers (Cuffey et al., 2000). So if the outlet valleys in our study area were cold-based, the depositional features never formed.

Nevertheless, the morphometry of the radiating valleys and the supposed polythermal regime also suggest that liquid water played a role in valleys development (section, 6.2; Fig.14f). In fact, the glacial valleys on the slope of the plateau become V-shaped, with a smaller V-index (< 0.1) at 25% of their length. These V-shaped and V-index values are characteristics of valleys shaped by a liquid erosive agent such as liquid water. In Bouquety et al. (2019), we discussed glaciated highlands at high elevation and temperate lowlands where the liquid water could have been stable. This liquid water could have come from the melting of the ice upstream (from the plateau ice cap or the supposed glacier front), and could have been a source and/or a reservoir for the valley networks at lowest elevation and fed the open-basin lake in this area (Fassett and Head, 2008a). This hypothesis seems to be consistent with the morphometrical results in this study.

Our study area includes an impact crater with inlet and outlet valleys. The inlet valleys are connected with the plateau area upstream, and downstream by an outlet valley to the lower elevations (Fig.23a, b). This structure could be categorized as an open-basin paleolake

following the established characteristics by Fassett and Head (2008a), namely a lake with outlet valleys, but it was not mapped. The two valleys from the plateau (Fig.23c and d), have the glacial properties described before but, as the majority of the radiating valleys, their V-index decreases downstream to the supposed open-basin paleolake (Fig.23b-d). In other words, the inlet valleys are U-shaped upstream and become V-shaped downstream approaching the open-basin paleolake. The cross-sectional profile at the transition between the open-basin paleolake and the outlet valley is V-shaped with a V-index of -0.07 and this valley is V-shaped all along with a mean V-index of 0.03 (Fig.23b, e), which is more similar to a fluvial valley than a glacial valley. In order to explain these morphologies, we propose that the two upstream valleys coming from the plateau are glacial. The supposed glaciers in these valleys could have melted during some subsequent warming phase and fed the depression downstream thus forming a lake in the crater. Then, the water in the lake flowed downstream following the slope to form the V-shaped valley. So the lake was fed by ice and/or meltwater from the glacier coming from the supposed plateau ice cap which indicates that ice (glacier) and liquid water (meltwater and/or subglacial water) could have coexisted. This hypothesis could be supported by the climatic model proposed by (Palumbo et al., 2018) which suggests the possibility of transient melting linked to fluvial and/or lacustrine activity through peak annual and seasonal temperatures during the cold and icy early Mars. Moreover, this observation is one more argument for the warm based regime of the radiating valleys coming from the plateau ice cap.

The glacial geomorphological evidence we bring here and in Bouquety et al. (2019) show that Terra Sabaea was, during the Late Noachian/Early Hesperian, a place with a complex glaciological history. The glacial landscape composed of glacial crater valleys, glacial cirques and a hypothesised former plateau ice cap show that the icy highland scenario predicted by the models is plausible (Wordsworth et al., 2013, Bouley et al., 2016). Nevertheless, the liquid water and the ice seems to be linked together, in fact the glacial morphologies in the highlands in Terra Sabaea seems to be connected with the fluvial morphologies downstream. Indeed, the presence of open-basin lakes (Fassett and Head, 2008a) and the catchment of Naktong vallis, located near Dawes crater (Fig.2), are dated at 3.6 Ga (Fassett2008, Bouley2009, Bouley and Craddock, 2014). The fact that these structures which are formed with liquid water (open basin lake and Naktong vallis) and glacial landscape are dated at the same age (3.6 Ga) seem to indicate that the water could have been liquid and solid during the same period of time. The elevation is an important factor to consider to study the link between the glacial and fluvial morphologies. The highlands in Terra Sabaea should be icy at high elevation (> 2500 m) and downstream, to the north, this ice could be a source of the fluvial morphologies at lower elevation (< 2500 m). Elsewhere on Mars evidence of Late Noachian/Early Hesperian glaciation have been demonstrated in Valles Marineris (Mège and Bourgeois, 2011, Gourronc et al., 2014) and in Tharsis volcanic province which acted like an ice trap through martian history (Cassanelli and Head, 2019). Combined, this evidence seems to show that the early martian climate was not uniquely warm, wet, or icy, but a combination of both with regional climate depending of the latitude, and elevation.

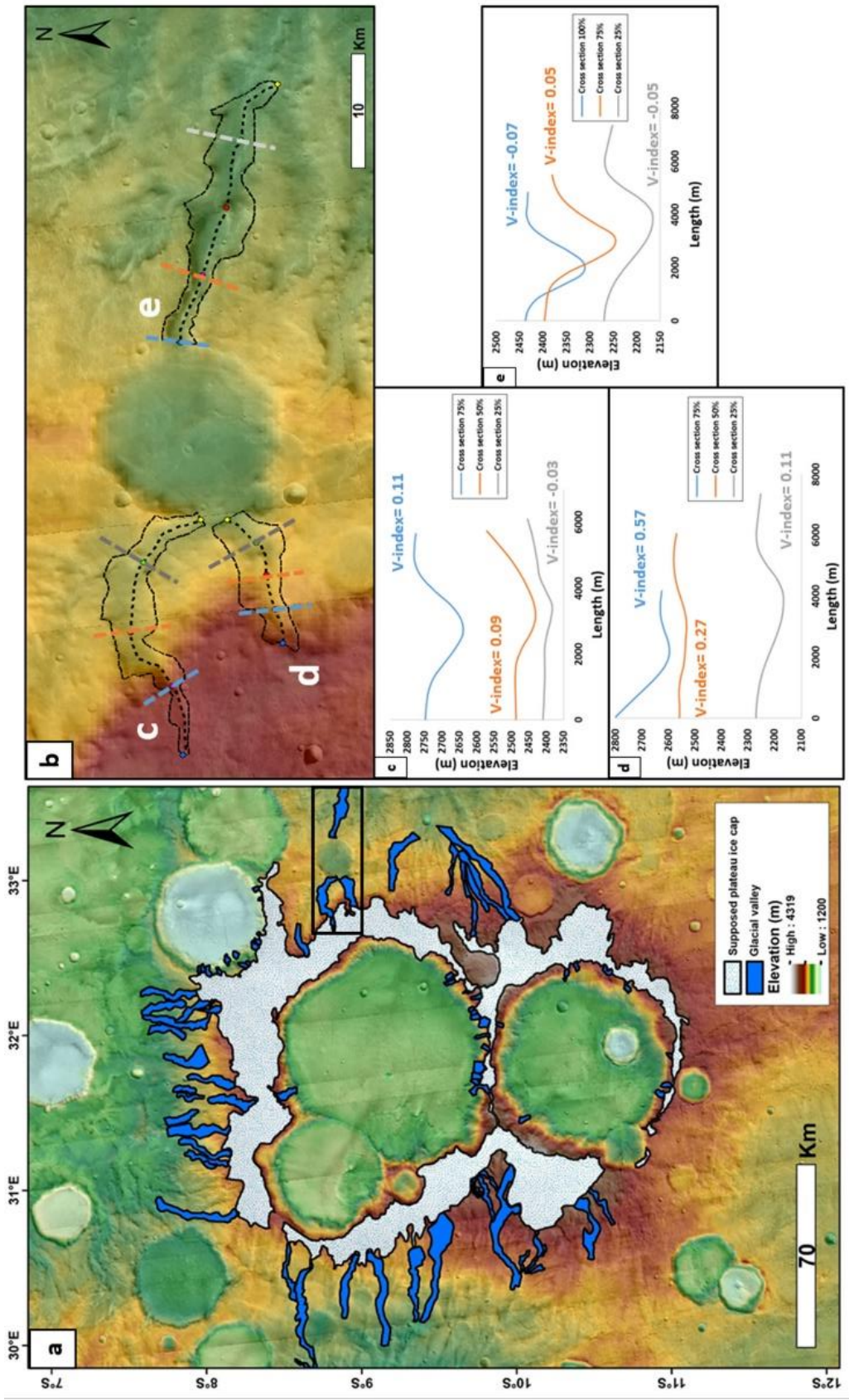

Figure 23: Supposed open-basin paleolake. (a) Study area (b) Zoom of the area represented by a black rectangle in (a). The white letter c, d and e represent the valley. The dashed colour lines are the location of the cross-sectional profiles show in (c), (e) and (f). CTX images with MOLA background. Images credit NASA/JPL/University of Arizona.

8 Conclusion

The morphometrical analyses allowed us to identify glacial valleys and a hypothesised former plateau ice cap located on a high plateau in Terra Sabaea at an elevation > 2500 m, this glacial landscape composed of glacial valleys and plateau ice cap, have morphological and geometrical similarities with glacial landforms on Earth. The crater-size frequency distributions give an age around 3.6 Ga. This age is consistent with the other demonstrated glacial landscape in this area (Bouquety et al., 2019) and in agreement with the icy highlands scenario predicted by the climate simulations (Wordsworth et al., 2013, Bouley et al., 2016). This study strongly supports the presence of a glaciated landscape in Terra Sabaea during the Late Noachian/Early Hesperian. Terra Sabaea proves to be an area with a complex glaciological history with the presence of a glacial landscape composed of glacial cirques, glacial valleys and a supposed plateau ice cap. The wide range of elevations and morphologies in Terra Sabaea seems to indicate that this area is a key place to understand the complex history of the early martian climate.

Acknowledgments

The authors acknowledge the HRSC Team of the German Aerospace Center (DLR) Berlin, who provided map projected HRSC DEM data and the CTX Team for the availability of the data on the web site http://ode.rsl.wustl.edu/mars/. We acknowledge the Orsay Planetary Picture Library for the data provided and image processing (http://fototek.geol.u-psud.fr). Authors are funded by the Programme National de Planétologie (PNP) of Centre National de la Recherche Scientifique/Institut National des Sciences de l'Univers, and the Centre National d'Etudes Spatiales (CNES). The authors also acknowledge Pierre Lahitte from GEOPS laboratory for the terrestrial DEM of the Cantal and Ping Fu from the University of Nottingham Ningbo, China for the terrestrial DEM of Shaluli Shan. The authors are very grateful to the two reviewers, Frances E.G. Butcher and the anonymous one, for their very constructive comments and suggestions that have improved the work presented here.

References

Amerson, B. E., Montgomery, D. R., Meyer, G., 2008. Relative size of fluvial and glaciated valleys in central idaho. Geomorphology 93 (3-4), 537_547, doi: 10.1016/j.geomorph.2007.04.001.

Anderson, R. S., Molnar, P., Kessler, M. A., 2006. Features of glacial valley profiles simply explained. Journal of Geophysical Research 111 (F1), doi: 10.1029/2005jf000344.

Andersson, G., 1998. Genesis of hummocky moraine in the bolmen area, southwestern sweden. Boreas 27 (1),55_67, doi: 10.1111/j.1502-3885.1998.tb00867.x.

Augustinus, P. C., 1992. Outlet glacier trough size-drainage area relationships, fjordland, new zealand. Geomorphology 4 (5), 347_361, doi: 10.1016/0169-555x(92)90028-m.

Barr, I. D., Spagnolo, M., 2015. Glacial cirques as palaeoenvironmental indicators: Their potential and
limitations. Earth-Science Reviews 151, 48_78, doi: 10.1016/j.earscirev.2015.10.004.

Bartholomew, I., Nienow, P., Sole, A., Mair, D., Cowton, T., King, M., Palmer, S., 2011a. Seasonal variations in greenland ice sheet motion: Inland extent and behaviour at higher elevations. Earth and Planetary Science Letters 307 (3-4), 271_278.

Bartholomew, I., Nienow, P., Sole, A., Mair, D., Cowton, T., Palmer, S., Wadham, J., 2011b. Supraglacial forcing of subglacial drainage in the ablation zone of the greenland ice sheet. Geophysical Research Letters

Bennett, M., Glasser, N., 2011. Glacial Geology: Ice Sheets and Landforms. Wiley.
URL https://books.google.fr/books?id=p6X0M5hAQj8C

Bibring, J.-P., Langevin, Y., Mustard, J. F., Poulet, F., Arvidson, R., Gendrin, A., Gondet, B., Mangold, N., Pinet, P., Forget, F., Berthe, M., Bibring, J.-P., Gendrin, A., Gomez, C., Gondet, B., Jouglet, D., Poulet, F., Sou_ot, A., Vincendon, M., Combes, M., Drossart, P., Encrenaz, T., Fouchet, T., Merchiorri, R., Belluci, G., Altieri, F., Formisano, V., Capaccioni, F., Cerroni, P., Coradini, A., Fonti, S., Korablev, O., Kottsov, V., Ignatiev, N., Moroz, V., Titov, D., Zasova, L., Loiseau, D., Mangold, N., Pinet, P., Doute, S., Schmitt, B., Sotin, C., Hauber, E., Ho_mann, H., Jaumann, R., Keller, U., Arvidson, R., Mustard, J. F., Duxbury, T., Forget, F., and, G. N., 2006. Global mineralogical and aqueous mars history derived from OMEGA/mars express data. Science 312 (5772), 400_404, doi: 10.1126/science.1122659.

Boule, M., 1896. La topographie glaciaire en auvergne. Annales de Géographie 5 (21), 277_296.

Bouley, S., Ansan, V., Mangold, N., Masson, P., Neukum, G., 2009. Fluvial morphology of naktong vallis, mars: A late activity with multiple processes. Planetary and Space Science 57 (8-9), 982_999, doi: 10.1016/j.pss.2009.01.015.

Bouley, S., Baratoux, D., Matsuyama, I., Forget, F., Séjourné, A., Turbet, M., Costard, F., 2016. Late Tharsis formation and implications for early mars. Nature 531 (7594), 344_347, doi: 10.1038/nature17171.

Bouley, S., Craddock, R. A., 2014. Age dates of valley network drainage basins and subbasins within
sabae and arabia terrae, mars. Journal of Geophysical Research: Planets 119 (6), 1302_1310, doi:
10.1002/2013JE004571.

Bouquety, A., Sejourne, A., Costard, F., Mercier, D., Bouley, S., 2019. Morphometric evidence of 3.6 ga glacial valleys and glacial cirques in martian highlands: South of terra sabaea. Geomorphology 334, 91_111, https://doi.org/10.1016/j.geomorph.2019.02.022.
URL http://www.sciencedirect.com/science/article/pii/S0169555X1930056X

Briner, J., Miller, G., Davis, P., Bierman, P., Ca_ee, M., 2003. Last glacial maximum ice sheet dynamics in arctic canada inferred from young erratics perched on ancient tors. Quaternary Science Reviews 22 (5-7),437_444.

Carr, M., 1995. The martian drainage system and the origin of valley networks and fretted channels. Journal of Geophysical Research 100 (E4), 7479, doi: 10.1029/95je00260.

Cassanelli, J. P., Head, J. W., 2019. Glaciovolcanism in the tharsis volcanic province of mars: Implications for regional geology and hydrology. Planetary and Space Science 169, 45 _ 69. URL http://www.sciencedirect.com/science/article/pii/S0032063318303192

Cowton, T., Nienow, P., Bartholomew, I., Sole, A., Mair, D., 2012. Rapid erosion beneath the greenland ice sheet. Geology 40 (4), 343_346.

Craddock, R. A., Howard, A. D., 2002. The case for rainfall on a warm, wet early mars. Journal of Geophysical Research: Planets 107 (E11), 21_1_21_36, doi: 10.1029/2001je001505.

Cuffey, K. M., Conway, H., Gades, A. M., Hallet, B., Lorrain, R., Severinghaus, J. P., Steig, E. J., Vaughn, B., White, J. W. C., 2000. Entrainment at cold glacier beds. Geology 28 (4), 351.

Davis, J., Balme, M., Grindrod, P., Williams, R., Gupta, S., aug 2016. Extensive noachian fluvial systems in arabia terra: Implications for early martian climate. Geology 44 (10), 847_850.

de Martonne, E., 1910. L'érosion glaciaire et la formation des vallées alpines. Annales de Géographie 19 (106), 289_317.

de Martonne, E., 1911. Fjords, cirques, vallées alpines et lacs subalpins. Annales de Géographie 10 (52), 289_294.
Derbyshire, E., Yafeng, S., Jijun, L., Benxing, Z., Shijie, L., Jingtai, W., 1991. Quaternary glaciation of tibet: The geological evidence. Quaternary Science Reviews 10 (6), 485_510, 10.1016/0277-3791(91)90042-s.

Durand, A., 1939. Notes sur le glaciaire dans le nord du cantal. Revue de géographie alpine 27 (4), 861_890, 10.3406/rga.1939.4109.

Etlicher, B., Hervé, A. D. G. D., 1988. La déglaciation würrmienne dans le massif central français, le point des travaux récents / the würmian déglaciation in the french massif-central, review of recent works,. Bulletin de l'Association française pour l'étude du quaternaire 25 (2), 103_110.

Evans, I. S., Cox, N. J., 2017. Comparability of cirque size and shape measures between regions and between researchers. Zeitschrift fur Geomorphologie, Supplementary Issues 61 (2), 81_103.

Ewertowski, M. W., Tomczyk, A. M., 2015. Quantification of the ice-cored moraines' short-term dynamics in the high-arctic glaciers ebbabreen and ragnarbreen, petuniabukta, svalbard. Geomorphology 234, 211_227, doi: 10.1016/j.geomorph.2015.01.023.

Fabel, D., Stroeven, A. P., Harbor, J., Kleman, J., Elmore, D., Fink, D., 2002. Landscape preservation under fennoscandian ice sheets determined from in situ produced 10be and 26al. Earth and Planetary Science Letters 201 (2), 397_406.

Fassett, C. I., Head, J. W., 2008a. The timing of martian valley network activity: Constraints from buffered crater counting. Icarus 195 (1), 61_89, doi: 10.1016/j.icarus.2007.12.009.

Fassett, C. I., Head, J. W., 2008b. Valley network-fed, open-basin lakes on mars: Distribution and implications for noachian surface and subsurface hydrology. Icarus 198 (1), 37_56, doi: 10.1016/j.icarus.2008.06.016.

Fassett, C. I., Head, J. W., Nov. 2008c. Valley network-fed, open-basin lakes on mars: Distribution and
implications for noachian surface and subsurface hydrology. Icarus 198 (1), 37_56.

Forget, F., Wordsworth, R., Millour, E., Madeleine, J.-B., Kerber, L., Leconte, J., Marcq, E., Haberle, R., 2013. 3d modelling of the early martian climate under a denser CO2 atmosphere: Temperatures and CO2 ice clouds. Icarus 222 (1), 81_99.

Fu, P., Harbor, J. M., Stroeven, A. P., Hättestrand, C., Heyman, J., Zhou, L., 2013a. Glacial geomorphology and paleoglaciation patterns in shaluli shan, the southeastern tibetan plateau _ evidence for polythermal ice cap glaciation. Geomorphology 182, 66_78.

Fu, P., Heyman, J., Hättestrand, C., Stroeven, A. P., Harbor, J. M., 2012. Glacial geomorphology of the shaluli shan area, southeastern tibetan plateau. Journal of Maps 8 (1), 48_55.

Fu, P., Stroeven, A. P., Harbor, J. M., Heyman, J., Hättestrand, C., Caffee, M. W., 2018. Ice cap erosion
patterns from bedrock 10 be and 26 al, southeastern tibetan plateau. Earth Surface Processes and
Landforms 44 (4), 918_932.

Fu, P., Stroeven, A. P., Harbor, J. M., Hättestrand, C., Heyman, J., Caffee, M. W., Zhou, L., 2013b. Paleoglaciation of shaluli shan, southeastern tibetan plateau. Quaternary Science Reviews 64, 121_135.

Gourronc, M., Bourgeois, O., Mège, D., Pochat, S., Bultel, B., Massé, M., Deit, L. L., Mouélic, S. L., Mercier, D., 2014. One million cubic kilometers of fossil ice in valles marineris: Relicts of a 3.5gy old glacial landsystem along the martian equator. Geomorphology 204, 235_255, doi: 10.1016/j.geomorph.2013.08.009.

Graf, W. L., 1970. The geomorphology of the glacial valley cross section. Arctic and Alpine Research 2 (4), 303, doi: 10.2307/1550243.

Gulick, V. C., 2001. Origin of the valley networks on mars: a hydrological perspective. Geomorphology 37 (3-4), 241_268, doi: 10.1016/s0169-555x(00)00086-6.

Gwinner, K., Jaumann, R., Hauber, E., Ho_mann, H., Heipke, C., Oberst, J., Neukum, G., Ansan, V., Bostelmann, J., Dumke, A., Elgner, S., Erkeling, G., Fueten, F., Hiesinger, H., Hoekzema, N., Kersten, E., Loizeau, D., Matz, K.-D., McGuire, P., Mertens, V., Michael, G., Pasewaldt, A., Pinet, P., Preusker, F., Reiss, D., Roatsch, T., Schmidt, R., Scholten, F., Spiegel, M., Stesky, R., Tirsch, D., van Gasselt, S.,Walter, S., Wählisch, M., Willner, K., 2016. The high resolution stereo camera (HRSC) of mars express and its approach to science analysis and mapping for mars and its satellites. Planetary and Space Science 126, 93_138, doi: 10.1016/j.pss.2016.02.014.

Hallet, B., Hunter, L., Bogen, J., 1996. Rates of erosion and sediment evacuation by glaciers: A review of field data and their implications. Global and Planetary Change 12 (1-4), 213_235.

Hargitai, H., Kereszturi, Á, 2015. Encyclopedia of Planetary Landforms. Springer New York.

Hartmann, W. K., 2005. Martian cratering 8: Isochron refinement and the chronology of mars. Icarus 174 (2), 294_320, doi: 10.1016/j.icarus.2004.11.023.

Hartmann, W. K., Neukum, G., 2001. Cratering chronology and the evolution of mars. Space Science Reviews 96 (1/4), 165_194, doi: 10.1023/a: 1011945222010.

Head, J. W., Marchant, D. R., 2014. The climate history of early mars: insights from the antarctic McMurdo dry valleys hydrologic system. Antarctic Science 26 (06), 774_800, doi: 10.1017/s0954102014000686.

Heyman, J., Hattestrand, C., Stroeven, A. P., 2008. Glacial geomorphology of the bayan har sector of the NE tibetan plateau. Journal of Maps 4 (1), 42_62.

Hobbs, S., Clarke, J., Paull, D., 2016. Analysis of crater valleys, noachis terra, mars: Evidence of fluvial and glacial processes. Geomorphology 261, 244_272, doi: 10.1016/j.geomorph.2016.02.027.

Hynek, B. M., Beach, M., Hoke, M. R. T., 2010. Updated global map of martian valley networks and implications for climate and hydrologic processes. Journal of Geophysical Research 115 (E9), doi: 10.1029/2009je003548.

Ivanov, B. A., 2001. Mars/moon cratering rate ratio estimates. In: Space Sciences Series of ISSI. Springer Netherlands, pp. 87_104, doi: 10.1007/978-94-017-1035-0.

Johnson, W. D., 1904. The profile of maturity in alpine glacial erosion. The Journal of Geology 12 (7), 569_578, doi: 10.1086/621181.

Kleman, J., Stroeven, A. P., 1997. Preglacial surface remnants and quaternary glacial regimes in northwestern sweden. Geomorphology 19 (1-2), 35_54.

Kneissl, T., van Gasselt, S., Neukum, G., 2011. Map-projection-independent crater size-frequency determination in GIS environments_new software tool for ArcGIS. Planetary and Space Science 59 (11-12), 1243_1254, doi: 10.1016/j.pss.2010.03.015.

Koppes, M. N., Montgomery, D. R., 2009. The relative efficacy of fluvial and glacial erosion over modern to orogenic timescales. Nature Geoscience 2 (9), 644_647

Kuhle, M., 1998. Reconstruction of the 2.4 million km2 late pleistocene ice sheet on the tibetan plateau and its impact on the global climate. Quaternary International 45-46, 71_108.

Larsen, E., Kjær, K., Demidov, I., Funder, S., Grøsfjeld, K., Houmark-Nielsen, M., Jensen, M., Linge, H.,Lyså, A., aug 2006. Late pleistocene glacial and lake history of northwestern russia. Boreas 35 (3), 394_424.

Livers, B., Wohl, E., 2015. An evaluation of stream characteristics in glacial versus fluvial process domains in the colorado front range. Geomorphology 231, 72_82, doi:10.1016/j.geomorph.2014.12.003.

Malin, M. C., Edgett, K. S., 2001. Mars global surveyor mars orbiter camera: Interplanetary cruise through primary mission. Journal of Geophysical Research: Planets 106 (E10), 23429_23570, doi: 10.1029/2000je001455.

Marsatwar, 2018. Mars at war. Nature Geoscience 11 (4), 219_219.
URL https://doi.org/10.1038/s41561-018-0107-7

Mège, D., Bourgeois, O., 2011. Equatorial glaciations on mars revealed by gravitational collapse of valles marineris wallslopes. Earth and Planetary Science Letters 310 (3-4), 182_191, doi: 10.1016/j.epsl.2011.08.030.

Michael, G., 2013. Planetary surface dating from crater size_frequency distribution measurements: Multiple resurfacing episodes and differential isochron fitting. Icarus 226 (1), 885_890.

Milankovitch, M., 1941. Kanon der erdbestrahlung und seine anwendung auf das eiszeitenproblem.

Montgomery, D. R., 2002. Valley formation by fluvial and glacial erosion. Geology 30 (11), 1047, doi:10.1130/0091-7613(2002)030<1047:vfbfag>2.0.co;2.

Moore, J. M., 2005. Large alluvial fans on mars. Journal of Geophysical Research 110 (E4), doi: 10.1029/2004je002352.

Palumbo, A. M., Head, J. W., Wordsworth, R. D., 2018. Late noachian icy highlands climate model: Exploring the possibility of transient melting and fluvial/lacustrine activity through peak annual and seasonal temperatures. Icarus 300, 261_286.

Penck, A., 1905. Glacial features in the surface of the alps. The Journal of Geology 13 (1), 1_19, doi: http://www.jstor.org/stable/30066319.
URL http://www.jstor.org/stable/30066319

Ramirez, R. M., 2017. A warmer and wetter solution for early mars and the challenges with transient warming. Icarus 297, 71_82, doi: 10.1016/j.icarus.2017.06.025.

Ramirez, R. M., Craddock, R. A., 2018. The geological and climatological case for a warmer and wetter early mars. Nature Geoscience 11 (4), 230_237, doi: 10.1038/s41561-018-0093-9.

Rea, B., Whalley, W., Evens, D., Gordon, J., McDougall, D., 1998. Plateau ice fields: Geomorphology and dynamics. Journal of Quaternary Science 13 (6), 35_54.

Roberts, M. C., Rood, K. M., 1984. The role of the ice contributing area in the morphology of transverse fjords, british columbia. Geografiska Annaler. Series A, Physical Geography 66 (4), 381_393, doi: http://www.jstor.org/stable/520858. URL http://www.jstor.org/stable/520858

Segura, T. L., 2002. Environmental effects of large impacts on mars. Science 298 (5600), 1977_1980, doi:10.1126/science.1073586.

Smith, D. E., Zuber, M. T., Frey, H. V., Garvin, J. B., Head, J. W., Muhleman, D. O., Pettengill, G. H., Phillips, R. J., Solomon, S. C., Zwally, H. J., Banerdt, W. B., Duxbury, T. C., Golombek, M. P., Lemoine, F. G., Neumann, G. A., Rowlands, D. D., Aharonson, O., Ford, P. G., Ivanov, A. B., Johnson, C. L., McGovern, P. J., Abshire, J. B., Afzal, R. S., Sun, X., 2001. Mars orbiter laser altimeter: Experiment summary after the first year of global mapping of mars. Journal of Geophysical Research: Planets 106 (E10), 23689_23722, doi: 10.1029/2000je001364.

Stroeven, A. P., Fabel, D., Hättestrand, C., Harbor, J., 2002. A relict landscape in the centre of fennoscandian glaciation: cosmogenic radionuclide evidence of tors preserved through multiple glacial cycles. Geomorphology 44 (1-2), 145_154.

Sugden, D. E., 1968. The selectivity of glacial erosion in the cairngorm mountains, scotland. Transactions of the Institute of British Geographers (45), 79.

Sugden, D. E., 1978. Glacial erosion by the laurentide ice sheet. Journal of Glaciology 20 (83), 367_391, https://doi.org/10.3189/S0022143000013915.

Sugden, D. E., Watts, S. H., 1977. Tors, felsenmeer, and glaciation in northern cumberland peninsula, baffin island. Canadian Journal of Earth Sciences 14 (12), 2817_2823.

Suggate, R., jan 1990. Late pliocene and quaternary glaciations of new zealand. Quaternary Science Reviews 9 (2-3), 175_197.

Tanaka, K. L., 1986. The stratigraphy of mars. Journal of Geophysical Research 91 (B13), E139, doi: 10.1029/jb091ib13p0e139.

Tanaka, K. L., Skinner, J. A., Dohm, J. M., Irwin, R. P., Kolb, E. J., Fortezzo, C. M., Platz, T., Michael, G. G., Hare, T. M., 2014. Geologic map of mars. Doi: 10.3133/sim3292.

Valadas, B., Veyret, Y., 1981. Englacement quaternaire et enneigement actuel de l 'aubrac et du cantal. Revue géographique des Pyrénées et du Sud-Ouest 52 (2), 201_215.

Veyret, Y., 1973. Note préliminaire à l'étude morphologique des marges du glacier de l'artense (massif central). Revue de géographie alpine 61 (2), 203_221.

Warner, N. H., Gupta, S., Calef, F., Grindrod, P., Boll, N., Goddard, K., jan 2015. Minimum effective area for high resolution crater counting of martian terrains. Icarus 245, 198_240.

Wordsworth, R., Ehlmann, B., Forget, F., Haberle, R., Head, J., Kerber, L., 2018. Healthy debate on early mars. Nature Geoscience 11 (12), 888_888.

Wordsworth, R., Forget, F., Millour, E., Head, J., Madeleine, J.-B., Charnay, B., 2013. Global modelling of the early martian climate under a denser CO2 atmosphere: Water cycle and ice evolution. Icarus 222 (1), 1_19, doi: 10.1016/j.icarus.2012.09.036.

Zemp, M., Haeberli, W., Paul, F., 2011. Vanishing glaciers in the european alps. Doi: 10.5167/uzh-83973.

Zimmer, P. D., Gabet, E. J., 2018. Assessing glacial modification of bedrock valleys using a novel approach. Geomorphology 318, 336_347, https://doi.org/10.1016/j.geomorph.2018.06.021

Supplementary material

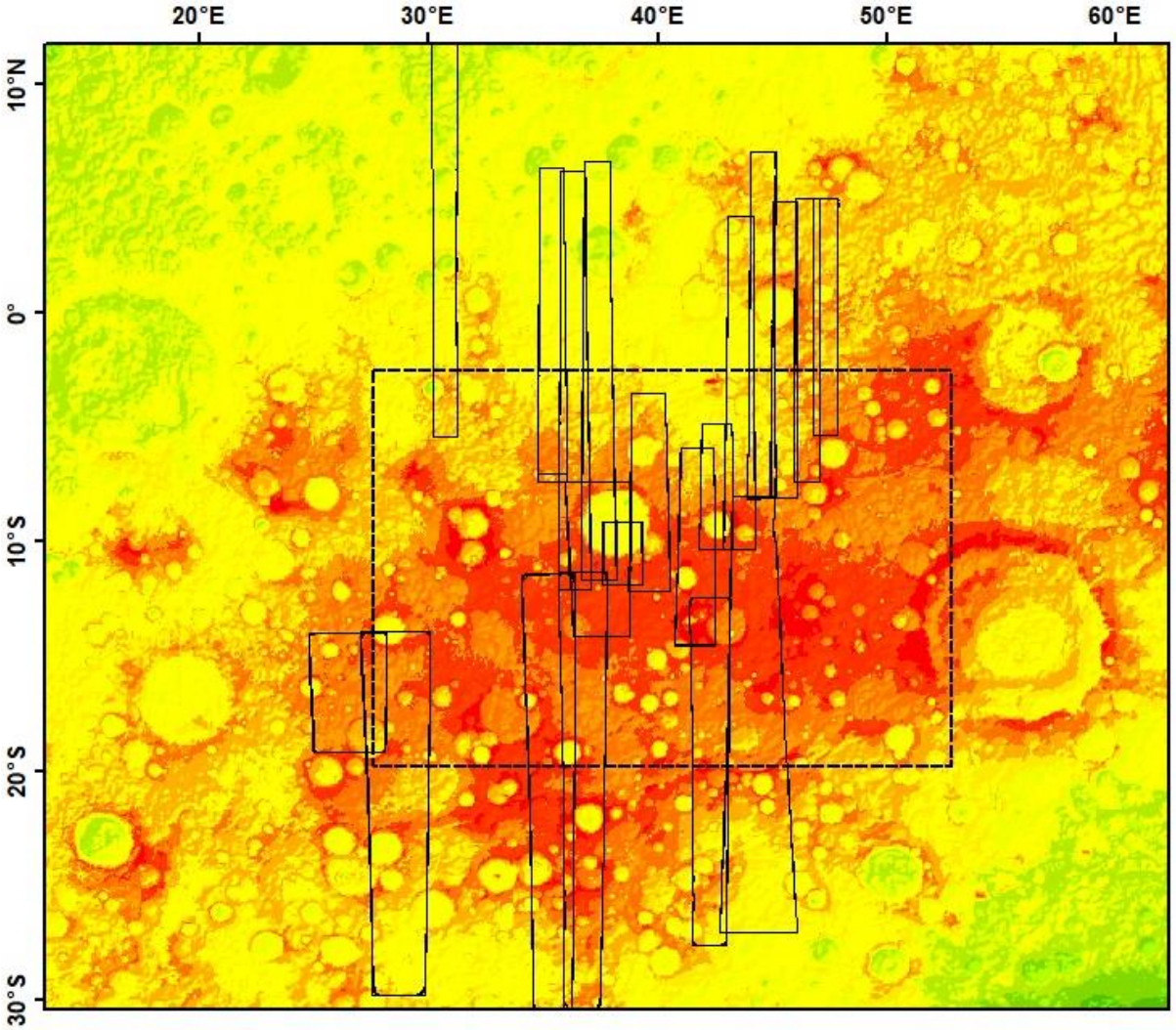

Figure 24: Data availability map. The black rectangles show the HRSC data available in our study area in the pointed rectangle

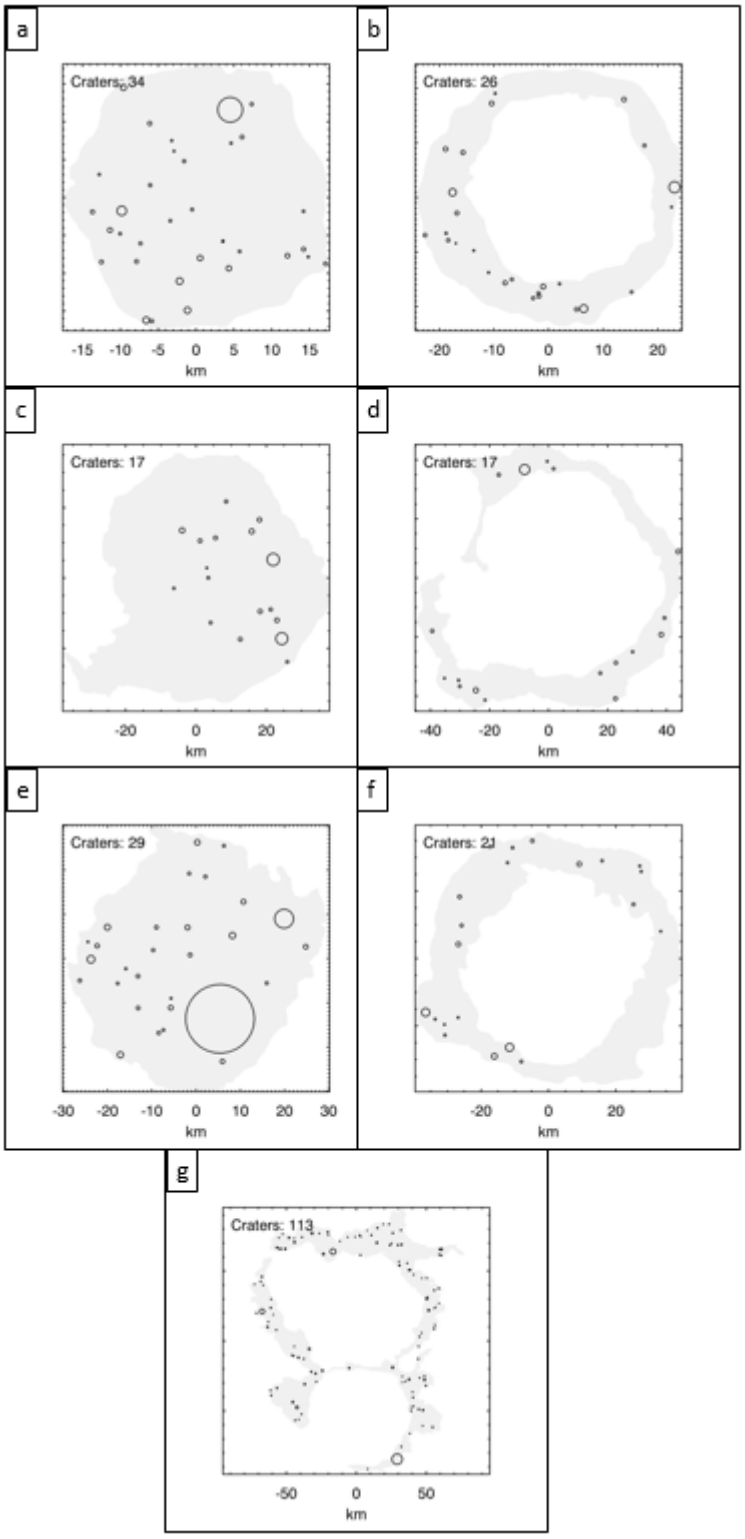

Figure 25: Map of the count-areas of craters > 1km. (a) Crater 2 floor. (b) Crater 2 inner walls. (c) Crater 3 floor (d) Crater 3 inner walls (e) Crater 4 floor (f) Crater 4 inner walls (g) Plateau area

N1/N2	2	3	4	5	6	7	8	9	10	11	12	13	14	15	16	17	18	19	20
2																		0	0
3								0	0	0	1	1	1	2	2	2	2	3	3
4					0	0	1	1	2	2	3	3	4	5	5	6	6	7	8
5				0	1	1	2	3	4	5	6	7	7	8	9	10	11	12	13
6			0	1	2	3	4	5	6	7	9	10	11	12	13	15	16	17	18
7			0	1	3	4	6	7	9	10	12	13	15	16	18	19	21	22	24
8			1	2	4	6	7	9	11	13	15	17	18	20	22	24	26	28	30
9		0	1	3	5	7	9	11	13	16	18	20	22	24	27	29	31	33	36
10		0	2	4	6	9	11	13	16	18	21	24	26	29	31	34	37	39	42
11		0	2	5	7	10	13	16	18	21	24	29	30	33	36	39	42	45	46
12		1	3	6	9	12	15	18	21	24	27	31	34	37	41	44	47	51	54
13		1	3	7	10	13	17	20	24	27	31	34	38	42	45	49	53	56	60
14		1	4	7	11	15	18	22	26	30	34	38	42	46	50	54	58	63	67
15		2	5	8	12	16	20	24	29	33	37	42	46	51	55	60	64	69	73
16		2	5	9	13	18	22	27	31	36	41	45	50	55	60	65	70	74	79
17		2	6	10	15	19	24	29	34	39	44	49	54	60	65	70	75	81	86
18		2	6	11	16	21	26	31	37	42	47	53	58	64	70	75	81	87	92
19	0	3	7	12	17	22	28	33	39	45	51	56	63	69	74	81	87	93	99
20	0	3	8	13	18	24	30	36	42	46	54	60	67	73	79	86	92	99	105
21	0	3	8	14	19	25	32	38	44	51	58	64	71	78	84	91	98	105	112
22	0	4	9	14	21	27	34	40	47	54	61	68	75	82	89	96	104	111	118
23	0	4	9	15	22	29	35	43	50	57	64	72	79	87	94	102	109	117	125
24	0	4	10	16	23	30	37	45	52	60	68	75	83	91	99	107	115	123	131
25	0	5	10	17	24	32	39	47	55	63	71	79	87	96	104	112	121	129	138
26	0	5	11	18	25	33	41	49	58	66	74	83	92	100	109	118	127	135	144
27	1	5	12	19	27	35	43	52	60	69	78	87	96	105	114	123	132	142	151
28	1	5	12	20	28	36	45	54	63	72	81	91	100	109	119	128	138	148	157
29	1	6	13	21	29	38	47	56	66	75	85	94	104	114	124	134	134	144	164
30	1	6	13	22	30	40	49	58	68	78	88	98	108	119	129	139	150	160	170
31	1	6	14	22	32	41	51	61	71	81	92	102	113	123	134	145	155	166	177
32	1	7	14	23	33	43	53	63	74	84	95	106	117	128	139	150	161	172	184
33	1	7	15	24	34	44	55	65	76	87	98	110	121	132	144	155	167	179	190
34	1	7	16	25	35	46	57	68	79	90	102	113	125	137	139	161	173	185	197
35	1	8	16	26	37	47	59	70	82	93	105	117	129	142	154	166	179	191	203
36	1	8	17	27	38	49	60	72	84	96	109	121	134	146	159	172	184	197	210
37	1	8	17	28	39	51	62	75	87	99	112	125	138	151	164	177	190	203	217
38	1	9	18	29	40	52	64	77	90	102	116	129	142	155	169	183	196	210	223
39	2	9	19	30	41	54	66	79	92	106	119	133	146	160	174	188	202	216	230
40	2	9	19	31	43	55	68	81	95	109	122	136	150	165	179	193	208	222	237

Table 7: Mann-Whitney table for a bilateral test.

Highlights

• Morphometric evidence of an ancient polythermal plateau ice cap in Terra Sabaea.
• Glacial landscape has an age of late Noachian/ early Hesperian at 3.6 Ga.
• Morphometric evidence of coexisting ice and liquid water.

Graphical abstract

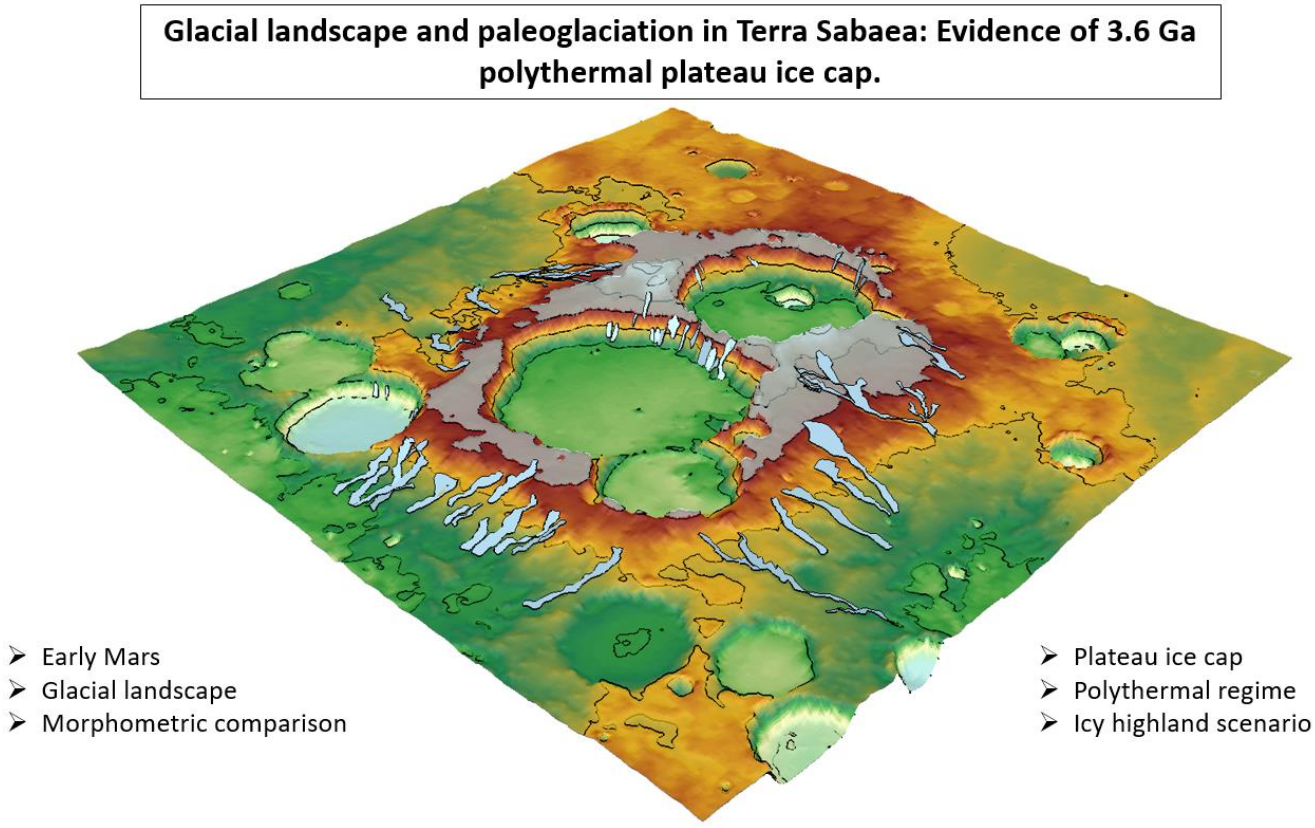

Figure 26: graphical abstract